Available online at www.sciencedirect.com

ScienceDirect

Journal of Nuclear Materials 366 (2007) 99–128

journal of nuclear materials

www.elsevier.com/locate/jnucmat

A conceptual model for the fuel oxidation of defective fuel

J.D. Higgs [a], B.J. Lewis [a,*], W.T. Thompson [a], Z. He [b]

[a] *Department of Chemistry and Chemical Engineering, Royal Military College of Canada, Kingston, Ont., Canada K7K 7B4*

[b] *Fuel Development Branch, Atomic Energy of Canada Limited-Chalk River Laboratories, Chalk River, Ont., Canada K0J 1J0*

Received 11 July 2006; accepted 19 December 2006

Abstract

A mechanistic conceptual model has been developed to predict the fuel oxidation behaviour in operating defective fuel elements for water-cooled nuclear reactors. This theoretical work accounts for gas-phase transport and sheath reactions in the fuel-to-sheath gap to determine the local oxygen potential. An improved thermodynamic analysis has also been incorporated into the model to describe the equilibrium state of the oxidized fuel. The fuel oxidation kinetics treatment accounts for multi-phase transport including normal diffusion and thermodiffusion for interstitial oxygen migration in the solid, as well as gas-phase transport in the fuel pellet cracks. The fuel oxidation treatment is further coupled to a heat conduction equation. A numerical solution of the coupled transport equations is obtained by a finite-element technique with the FEMLAB 3.1 software package. The model is able to provide radial–axial profiles of the oxygen-to-uranium ratio and the fuel temperatures as a function of time in the defective element for a wide range of element powers and defect sizes. The model results are assessed against coulometric titration measurements of the oxygen-to-metal profile for pellet samples taken from ten spent defective elements discharged from the National Research Universal Reactor at the Chalk River Laboratories and commercial reactors.

1. Introduction

With a defective fuel element, the sheath no longer provides a barrier between the fuel and primary coolant (see Fig. 1). Coolant can therefore contact the fuel, permitting oxidation of both the fuel and inner surface of the sheath. Fission products (FPs) and fuel grains can further escape into the primary heat transport system (PHTS) [1]. The presence of water vapour in the fuel-to-sheath gap can lead to a degradation in the thermal performance of the fuel element [2]. For instance, the gap heat transfer coefficient will change as steam and hydrogen replace the helium fill gas [2,3]. The fuel oxidation process itself can lead to a degraded thermal conductivity in the hyperstoichiometric fuel and a lower incipient melting temperature [4–7]. The release behaviour of fission products from the fuel element may also be enhanced due to a greater mobility of FPs in the hyperstoichiometric fuel [8].

The effect of changing oxygen potential in the fuel, and the related oxygen-to-metal (O/M) ratio

---

[*] Corresponding author. Tel.: +1 613 541 6611; fax: +1 613 542 9489.

E-mail address: lewis-b@rmc.ca (B.J. Lewis).

0022-3115/$ - see front matter © 2007 Elsevier B.V. All rights reserved.
doi:10.1016/j.jnucmat.2006.12.050

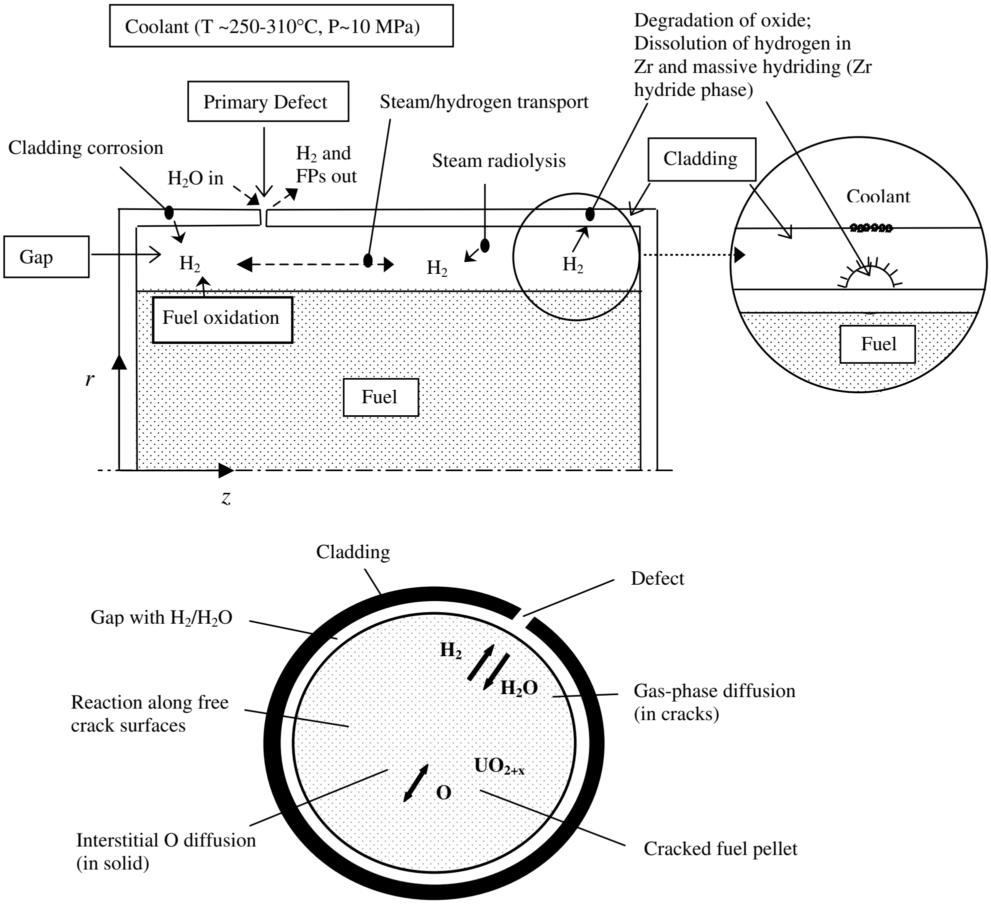

Fig. 1. Schematic of physical/chemical processes in defective fuel. Sources of hydrogen and gas-phase transport in the element (upper figure), and cross section of a defective element showing interstitial oxygen diffusion in the solid fuel matrix and gas-phase transport of hydrogen/steam in the fuel cracks (lower figure).

of the fuel, has been investigated as a function of burnup for intact fuel rods. For instance, Kelykamp calculated the compositional change of stoichiometric UO_2 fuel at an enrichment of 4.3 at.% ^{235}U, where it was suggested that the fuel O/M remains close to stoichiometry during irradiation (i.e., up to a burnup of 5 at.%) due to the oxygen-gettering effect of the cladding [9]. Measurements have also been made of the oxygen potential of irradiated UO_2 fuel [10–12]. Detailed measurements have been recently obtained by Walker et al., at an ultra-high burnup of ~10 at.%, which included the oxygen potential using a galvanic cell, the local oxygen-to-uranium (O/U) ratio based on the lattice parameter with micro-X-ray diffraction, and the local O/M by ICP-MS [13]. In addition, some limited measurements have been carried out on irradiated fuel specimens from defective commercial fuel rods [14–16].

Although simple models have been developed to describe the fuel oxidation kinetics in operating fuel rods [2,5–7], these treatments specifically ignore the axial migration of steam/hydrogen in the fuel-to-clad gap (i.e., gap oxygen potential). Moreover, these analyses neglect the effect of interstitial oxygen migration due to axial diffusion and thermodiffusion in a temperature gradient. A more mechanistic conceptual model is developed in this work to predict fuel oxidation behaviour in operating defective fuel elements in order to better assess the thermal performance of defective fuel. The model has also been assessed using recent O/M measurements for pellet samples taken from spent defective fuel elements based on a coulometric titration method as performed at the Chalk River Laboratories (CRL). This work therefore provides an understanding on how defective fuel behaves and what parameters control this behaviour.

2. Model development

Modelling of the interrelated processes for fuel oxidation and sheath oxidation/hydriding in Fig. 1 is a complicated problem. A treatment is required for both gas phase and solid-state diffusion, which are controlled by temperature-dependent reactions (that necessitates knowledge of the temperature distribution in the fuel element). Fuel oxidation is controlled by vapour transport in the fuel-to-sheath gap, and subsequently into the cracks of the fuel pellets where this surrounding atmosphere is in contact with the solid fuel matrix. The current model is applied to fuel conditions for the Canada Deuterium Uranium (CANDU™) system. In the following discussion, reference will only be made to hydrogen (H_2) and steam (H_2O) but this discussion also pertains in an equivalent manner to D_2 and D_2O for the heavy water system (Appendix A.1).

2.1. Gas phase transport in the fuel-to-sheath gap

The partial pressure ratio of hydrogen-to-steam (H_2/H_2O), $q/(1-q)$, yields the oxygen potential in the gap. The breached location provides a site for coolant entry into the defective element where steam can migrate along the fuel-to-sheath gap by gas-phase diffusion. The composition of the gas phase will consist of a steam/hydrogen mixture due to the liberation of hydrogen as a result of steam oxidation of the Zircaloy sheathing and fuel. This process will introduce counter-current transport of gaseous hydrogen towards the defect site. In addition, multiple defect sites in a fuel element can also result in a bulk flow of gas in the gap due to a pressure drop between the various defect locations.

During normal operation, the fission gas constituent (i.e., xenon and krypton) of the gas mixture is generally negligible. Hence, one need only consider the hydrogen species since the mole fraction of the hydrogen and steam sum approximately to unity. Thus, the mass balance for the hydrogen molar concentration (qc_g) in the gap can be given generally by [17]:

$$\frac{\partial(qc_g)}{\partial t} + \vec{\nabla}\cdot(qc_g\vec{u}) = \vec{\nabla}\cdot(c_gD_g\vec{\nabla}q) + \sigma_g(\{1-f\}R^{ox}_{clad,Zry} + R_{fuel}), \qquad (1)$$

where c_g is the total molar concentration of gas in the gap (mol m^{-3}) ($=p_t/(RT_g)$ for an ideal gas law with a system pressure p_t (atm), average gap temperature T_g (K) and ideal gas constant (R)), q is the hydrogen mole fraction of the gas and σ_g is the surface-to-volume ratio of the gap (m^{-1}). The diffusivity quantity c_gD_g (mol m^{-1} s^{-1}) can be evaluated from the Chapman–Enskog kinetic theory [7,17,18]. The source term $R^{ox}_{clad,Zry}$ accounts for the production rate of hydrogen due to the sheath corrosion reaction (in mol H_2 cm^{-2} s^{-1}), which is a function of the sheath temperature T_s (K) [1,19]:

$$R^{ox}_{clad,Zry} = 1.60\times10^{-2}\exp\{-14\,192/T_s\}F, \qquad (2)$$

where the enhancement factor for in-reactor corrosion is $F\sim 49$ [1]. A hydrogen pick-up fraction $f = 0.05$ for the sheath can be further assumed [20]. The term R_{fuel} is the additional source of hydrogen from the fuel oxidation reaction, which is obtained from the Fick's law of diffusion (i.e., as evaluated at the pellet surface, $r = a$):

$$R_{fuel} = -\left[c_gD_g\varepsilon\frac{\partial q}{\partial r}\right]_{r=a}, \qquad (3)$$

where ε is the crack porosity in the fuel pellet. An axial bulk-flow molar velocity $\vec{u} = u\hat{z}$(m s^{-1}) may occur along the gap depending on the axial location of the defects, i.e., a pressure gradient will exist between defects located at different axial locations as a result of a pressure drop Δp for the primary coolant due to frictional losses along the fuel bundle. Thus, for an incompressible Bernoulli flow, accounting for a pressure drop through only the small primary defect and along the gap, the axial bulk-flow velocity is given by [20,21]:

$$u = \sqrt{\Delta p}\left[f_r\rho\frac{\Delta l}{4t_g} + \frac{k_L\rho}{2}\left(\frac{A_1}{A_2}\right)^2\right]^{-1/2}, \qquad (4)$$

where f_r is a friction factor (∼0.015), ρ is the average density of the gas mixture, t_g is the radial gap thickness, Δl is the distance between the primary and secondary defects, k_L is the loss coefficient for a sudden contraction (0.5) or expansion (1.0), A_2 is the cross sectional area through the primary defect and A_1 is the cross sectional area through the gap. A contraction or expansion will occur depending on whether the primary defect occurs downstream or upstream of the secondary failure. Since the gap thickness in the operating fuel element is many orders of magnitude smaller than the element radius, and the fuel-stack length is much longer than the radius, the gas transport in the gap can be modelled as a one-dimensional (axial) geometry. Therefore, if the total molar concentration of gas in the fuel-to-sheath gap is constant with time, Eq. (1) can be written as:

$$c_g \frac{\partial q}{\partial t} = \frac{\partial}{\partial z}\left(c_g D_g \frac{\partial q}{\partial z}\right) - \frac{\partial}{\partial z}(q c_g u) + \sigma_g(\{1-f\}R^{ox}_{clad,Zry} + R_{fuel}). \quad (5)$$

Even if there is no pressure gradient along the gap, a total gas velocity will arise due to removal of hydrogen by the sheath, with a pickup fraction of $f \sim 5\%$ of the reaction rate $R^{ox}_{clad,Zry}$. On the other hand, fission gas is released into the fuel-to-clad gap (q_{fg}) (mol m^{-3} s^{-1}), which will counter-balance the hydrogen loss. The total gas balance in the gap is therefore

$$\frac{\partial(c_g u)}{\partial z} = -\frac{f R^{ox}_{clad,Zry}}{t_g} + q_{fg}. \quad (6)$$

However, the fission gas release during normal reactor conditions is typically small and does not impact the transport in the gap [22]. In addition, the hydrogen mole fraction in the gap is typically small (Section 3). Hence, these opposing effects are neglected and only the pressure gradient effect along the gap is considered in the current analysis.

2.2. Interstitial oxygen diffusion in the fuel matrix

Several mechanisms can affect the redistribution of oxygen in operating reactor oxide fuel elements as observed, for example, in uranium–plutonium mixed oxides. It has been suggested that the transport of oxygen can occur via [23]: (i) gas phase equilibrium (as suggested by Rand and Markin) involving CO/CO$_2$ and H$_2$/H$_2$O gas mixtures existing particularly in cracks and channels of interconnected porosity within the fuel [24]; and (ii) thermodiffusion (i.e., Soret effect) of oxygen vacancies and interstitials (as suggested by Sari and Schumacher) [25,26]. With fuel of higher density (e.g., ~97% theoretical density), gas phase transport of CO/CO$_2$ should be less pronounced. Moreover, in the plastic region of the fuel pellet, this latter process cannot occur where cracks produced by thermal shock should heal in a relatively short period of time by the condensation of fuel material. Hence, mechanism (i) is less likely and is therefore not considered in the current treatment.

Considering the fuel oxidation/reduction reaction:

$$UO_2 + xH_2O \leftrightarrow UO_{2+x} + xH_2 \quad (7)$$

and accounting for both normal diffusion and diffusion in a temperature gradient (Soret effect), the generalized mass balance for oxygen transport in the fuel matrix in Fig. 1 is given by [20,25]:

$$c_U \frac{\partial x}{\partial t} = c_U \vec{\nabla} \cdot \left(D\left(\nabla x + x\frac{Q}{RT^2}\nabla T\right)\right) + \sigma_f R^{react}_f. \quad (8)$$

Here c_U (mol m^{-3}) is the molar density of uranium, σ_f is the surface area of cracks per unit volume of fuel (m^{-1}) for the cracked fuel body and R^{react}_f is the rate of reaction for either fuel oxidation or reduction. Using a surface-exchange model, the kinetic reaction rates (in moles O (or H$_2$) m^{-2} s^{-1}) for fuel oxidation is given as [7,27–30]:

$$R^{react}_f = c_U \alpha \sqrt{(1-q)p_t}(x_e - x), \quad \text{for } x < x_e \quad (9)$$

The parameter $\alpha = 36.5\exp\{-23\,500/T\}$ is the rate coefficient for the surface-exchange of oxygen (cm s^{-1}) at the fuel temperature T (K) [27,28], x_e is the equilibrium stoichiometry deviation based on the local oxygen potential of the gas in the fuel cracks, x is the deviation from stoichiometry in UO$_{2+x}$ and p_t is the total system pressure (atm). The diffusion coefficient for the oxygen interstitials D can be evaluated from the chemical diffusion coefficient [31]:

$$D = 2.5\exp(-16\,400/T)\ \text{cm}^2\ \text{s}^{-1}, \quad (10)$$

where the temperature T is in K. The molar effective heat of transport Q is taken from the oxygen redistribution model (OXIRED) (i.e., for (U, Pu)O$_{2+x}$) in the TRANSURANUS code [26]:

$$Q = -3.5 \times 10^{34}\exp\{-17(4+2x)\}\ \text{J mol}^{-1} \quad (11)$$

which can be adopted for UO$_{2+x}$ since Q is shown to have a weak dependence on the plutonium content [25,32]. Moreover, one can assume a similar thermal diffusion ratio k_T for the two ceramics, and since the chemical oxygen diffusivities in (U, Pu)O$_{2+x}$ and UO$_{2+x}$ are similar (especially at higher temperatures) as seen in Fig. 13 of Ref. [33], the Q value should therefore be comparable.

The equilibrium stoichiometry deviation x_e follows from an equilibrium thermodynamic analysis for the uranium–oxygen system (see Appendix A) [34–59]:

$$x_e = \left(\frac{a + c\zeta + eT + g\zeta^2 + mT^2 + k\zeta T}{1 + b\zeta + dT + f\zeta^2 + pT^2 + n\zeta T}\right), \quad (12)$$

where $a = 0.033107$, $b = 0.268985$, $c = 0.0086795$, $d = -6.222 \times 10^{-4}$, $e = -5.188 \times 10^{-5}$, $f = 0.020038$, $g = 4.5017 \times 10^{-4}$, $k = -7.8344 \times 10^{-6}$, $m = 1.842 \times 10^{-8}$, $n = -7.452 \times 10^{-5}$, $p = 1.3906 \times 10^{-7}$, and $\zeta = \log\left(\frac{q}{1-q}\right)$. Here q is the H_2 mole fraction in the fuel cracks as evaluated with Eq. (15) in Section 2.3. As shown in Appendix A, there is very little difference in the estimate of the equilibrium stoichiometry deviation between light and heavy water. Thus, any thermodynamic analysis for light water can be applied to the heavy water CANDU system (using appropriate binary diffusion coefficients in the kinetic model). In addition, as further discussed in Appendix A, burnup effects can be neglected since the degree of oxygen binding to the fuel is small at typical CANDU fuel burnups.

Oxygen transport in the solid fuel matrix can occur in both the radial and axial direction, so that Eq. (8) can be written as:

$$c_U \frac{\partial x}{\partial t} = c_U \frac{\partial}{\partial z}\left(D \frac{\partial x}{\partial z}\right) + c_U \frac{1}{r}\frac{\partial}{\partial r}\left[rD\left(\frac{\partial x}{\partial r} + x\frac{Q}{RT^2}\frac{\partial T}{\partial r}\right)\right] + \sigma_f R_f^{\text{react}}. \tag{13}$$

2.3. Gas phase transport in the fuel cracks

The fuel oxidation reaction contributes hydrogen to the gas environment in the fuel cracks in Fig. 1. The hydrogen-to-steam partial pressure ratio in the fuel cracks, $q/(1-q)$, provides a boundary condition for the atmospheric oxygen potential in equilibrium with the solid, which controls x_e as shown in Section 2.2 above. The cracked solid is assumed to have a porosity ε, defined as the ratio of the volume of cracks (and/or pores) to the volume of the solid fuel i.e., $V_{\text{cracks}}/V_{\text{fuel}}$. Hence, the mass balance for the hydrogen molar concentration (qc_g) in the fuel cracks is given by [7,20]:

$$\varepsilon \frac{\partial (qc_g)}{\partial t} = \varepsilon \vec{\nabla} \cdot (c_g D_g \vec{\nabla} q) + \sigma_f R_f^{\text{react}}. \tag{14}$$

Since axial transport of hydrogen in the gap is a more effective path compared to that in the fuel cracks, only radial transport of hydrogen in the cracks is considered in the model. Thus, using a tortuosity factor τ for the diffusion path in the cracked solid, Eq. (14) can be simplified to:

$$\varepsilon c_g \frac{\partial q}{\partial t} = \frac{\varepsilon}{\tau^2 r}\left[\frac{\partial}{\partial r}\left(r c_g D_g \frac{\partial q}{\partial r}\right)\right] + \sigma_f R_f^{\text{react}}. \tag{15}$$

2.4. Heat conduction in the solid

The solution of Eqs. (5), (13) and (15) requires a specific knowledge of the temperature distribution in the fuel element since the reaction rates and transport terms are temperature dependent. In addition, consideration must be given to any reduced heat transfer in the fuel-to-sheath gap (due to the presence of steam in the gap) and the feedback effect due to a reduced thermal conductivity in the hyperstoichiometric fuel.

The sheath outside temperature (T_{so}), sheath inside temperature (T_{si}) and fuel surface temperature (T_{fs}) are calculated in the current work based on a Maple analysis [59]. The fuel surface temperature is required as a boundary condition for the heat conduction model in the fuel. The sheath inside and outside temperatures provide an estimate of the average sheath temperature (T_s), which is used in Eq. (2). The temperature profile in the fuel element is obtained from the solution of the general time-dependent heat conduction equation [60]:

$$\rho_s C_p \frac{\partial T}{\partial t} = \vec{\nabla} \cdot (k \vec{\nabla} T) + Q_v, \tag{16}$$

where ρ_s is the fuel density, C_p is the specific heat of the fuel, k is the thermal conductivity of the fuel and Q_v is the volumetric source term. Thus, considering both axial and radial heat conduction and flux depression, Eq. (16) can be rewritten as [20]:

$$\rho_s C_p \frac{\partial T}{\partial t} = \frac{\partial}{\partial z}\left(k \frac{\partial T}{\partial z}\right) + \frac{1}{r}\frac{\partial}{\partial r}\left(rk\frac{\partial T}{\partial r}\right) + \frac{P}{\pi a^2}\left[\frac{(\kappa a)}{2I_1(\kappa a)}\right] I_0(\kappa r), \tag{17}$$

where P is the linear power of the fuel element (kW m^{-1}), a is the pellet radius (m) and κ is the inverse neutron diffusion length (m^{-1}). Eq. (17) is further coupled to Eqs. (13) and (15) because the thermal conductivity, k, is also a function of the stoichiometry deviation, x, as described below. A time-dependent model for heat conduction is considered so that the current treatment can be eventually extended for transient conditions, to determine if fuel centerline melting can occur in defective fuel during a power pulse [32]. For instance, the ratio of the thermal diffusivity-to-mass diffusivity can be interpreted as the time required for the stoichiometry deviation field to reach steady-state compared to the time for the temperature field to reach its equilibrium state. Since this ratio varies greatly, this disparity in the characteristic times of heat and oxygen diffusion can play an important role in the transient behaviour of fuel under sudden changes in operating conditions [32].

The specific heat capacity C_p (in J mol^{-1} K^{-1}), as a function of temperature T (K) and x, follows from the thermodynamic treatment:

$$\begin{aligned} C_p(x,T) = {} & 52.174 + 45.806x + (87.951 \times 10^{-3} \\ & - 7.3461 \times 10^{-2}x)T \\ & + (1-x)\{-84.241 \times 10^{-6}T^2 + 31.542 \\ & \times 10^{-9}T^3 - 2.6334 \times 10^{-12}T^4\} \\ & - (713910 + 295090x)T^{-2} \qquad (18) \end{aligned}$$

The density of the fuel ρ_s (kg m^{-3}) can be taken for that of stoichiometric urania as a function of temperature T (K) [61]:

$$\rho_s(T) = \begin{cases} \rho_s(273\,\mathrm{K}) \times (0.99734 + 9.802 \times 10^{-6}T - 2.705 \times 10^{-10}T^2 + 4.391 \times 10^{-13}T^3)^{-3}, & 273 < T < 923\,\mathrm{K} \\ \rho_s(273\,\mathrm{K}) \times (0.99672 + 1.179 \times 10^{-5}T - 2.429 \times 10^{-9}T^2 + 1.219 \times 10^{-12}T^3)^{-3}, & T \geqslant 923\,\mathrm{K}. \end{cases} \qquad (19)$$

The fuel thermal conductivity in UO_{2+x} can be evaluated from the general relation [62]:

$$k = \kappa_{1d}\kappa_{1p}\kappa_{2p}\kappa_{4r}(k_{ph} + k_e + k_{rad}), \qquad (20)$$

where k_{ph} accounts for conductive heat transfer via lattice vibration (phonons), k_e results from electron-hole movement (polarons) and k_{rad} considers radiative thermal effects. The other terms provide corrections for burnup and porosity effects where κ_{1d} is due to the dissolved fission products, κ_{1p} arises for the precipitated fission products, κ_{4r} is for radiation damage and κ_{2p} accounts for fuel porosity. For normal operating fuel temperatures, the radiative thermal conductivity term, k_{rad}, contributes less than 0.01% to the overall thermal conductivity and can therefore be neglected.

The phonon contribution (k_{ph}) is generally dominant and results from the scattering of phonons with lattice defects and phonon self-scattering for temperatures below 3000 K. This latter component is a function of the stoichiometry deviation of the fuel and its impurity content. The Ellis–Porter–Shaw model was therefore used for k_{ph} over the stoichiometry deviation range from $x = 0$ to ~0.2 (i.e., for fully-dense fuel) [63]:

$$k_{4ph} = \frac{1}{A(x) + B(x)T}\ \mathrm{kW\ m^{-1}\ K^{-1}}. \qquad (21)$$

Here T is the fuel temperature in K and the coefficients A and B are given by:

$$A(x) = 14 - 10.763\sqrt{x} - 2381.4x + 12819.86(\sqrt{x})^3, \qquad (22a)$$

$$B(x) = \begin{cases} 0.2218 + 0.2562\sqrt{x} - 0.64x \\ \quad -3.6764(\sqrt{x})^3, & x < 0.155 \\ 0, & x \geqslant 0.155. \end{cases} \qquad (22b)$$

The electronic contribution is based on the model of Ronchi [64]:

$$\begin{aligned} k_e = {} & (0.871 + 2.5 \times 10^{-5}T)^{-1}\frac{2.024 \times 10^8}{T^{5/2}} \\ & \times \exp\{-16350/T\}\ \mathrm{kW\ m^{-1}\ K^{-1}}, \qquad (23) \end{aligned}$$

which has been corrected to fully dense fuel using the Loeb expression [65]:

$$\kappa_{2p} = (1 - \beta_T P_{or}). \qquad (24)$$

The parameter β_T accounts for the temperature effect where $\beta_T = 2.6 - 0.5 \times 10^{-3}T$ (K) [66]. The porosity, P_{or}, is evaluated from the expression:

$$P_{or} = (1 - \rho_s/\rho_{TD})(1 - F_d), \qquad (25)$$

where ρ_s is the density of the fuel and ρ_{TD} is the theoretical density of UO_2 (10.96 g cm^{-3}). To account for fuel densification effects during operation, the initial manufactured porosity can be modified with the term $(1 - F_d)$, where F_d is the fractional change in porosity that is a function of temperature T (K) and burnup B (MWh (kgU)$^{-1}$) [67]:

$$\begin{aligned} F_d = {} & 0.6 - \exp\{-0.506 - 8.67 \times 10^{-10}T^3 \\ & \times [1 - \exp(-2.87 \times 10^{-2}B)]\}. \qquad (26) \end{aligned}$$

The correction factor for fully dense fuel for the dissolved fission products at a burnup β (atom %) is given by [62]:

$$\begin{aligned} \kappa_{1d} = {} & \left(\frac{1.09}{\beta^{3.265}} + \frac{0.0643}{\sqrt{\beta}}\sqrt{T}\right) \\ & \times \arctan\left(\frac{1}{1.09/\beta^{3.265} + (0.0643/\sqrt{\beta})\sqrt{T}}\right), \qquad (27) \end{aligned}$$

while for the precipitated fission products:

$$\kappa_{1\mathrm{p}} = 1 + \frac{0.019\beta}{(3-0.019\beta)(1+\exp\{-(T-1200)/100\})}. \tag{28}$$

The conversion factor for the burnup unit of β is 1 atom% $\sim$225 MWh $(\mathrm{kgU})^{-1}$. For typical CANDU fuel burnups, the correction for the dissolved and precipitated fission products is negligible. The effects of radiation damage are important only for temperature below about 1100 K (due to annealing effects above this temperature), where

$$\kappa_{4\mathrm{r}} = 1 - \frac{0.2}{1+\exp((T-900)/80)}. \tag{29}$$

The Lucuta formalism can be compared to a simple formula developed for irradiated UO_2 based on the Halden Research Project with fuel instrumented with thermocouples for 95% theoretical density up to a burnup of 67 MWd/kgU [68,69]. The Halden measurements for irradiated fuel indicate a larger reduction in thermal conductivity with burnup than that suggested for the SIMFUEL correlation. However, this difference is of less importance for the much lower burnups experienced by CANDU fuel. The Lucuta formalism is therefore adopted in the current analysis since it is more easily adapted for incorporation of fuel oxidation effects.

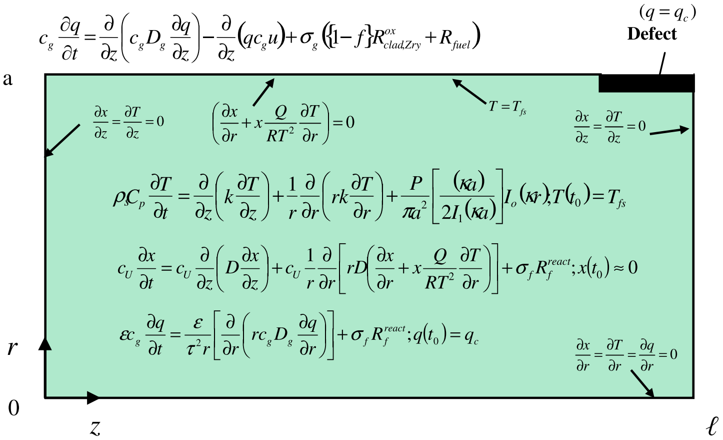

Fig. 2. Equations, boundary conditions and initial conditions for the two-dimensional defective fuel element model (not to scale).

Table 1
List of constants used for the FEMLAB simulation

Symbol	Description	Value
a	CANDU pellet radius for 37/28 element fuel	6.075×10^{-3} m/7.15×10^{-3} m
P	Linear power density	28 kW/m[a]
σ_f	Pellet average surface-to-volume ratio	910 m^{-1}
κ	Inverse neutron diffusion length	110 m^{-1}
ε	Fuel pellet porosity	0.015
R	Universal gas constant	8.205×10^{-5} m^3 atm mol^{-1} K^{-1}
p_t	Total system pressure	100 atm
c_u	U molar density	4.1×10^4 $\mathrm{mol/m}^3$
τ	Tortuosity factor	1.00
T_g	Average gap temperature	623 K[a]
q_c	Hydrogen molar fraction in coolant	4.1×10^{-6}
x_{fs}	Stoichiometry deviation at pellet surface	1×10^{-4}
T_b	Bulk coolant temperature	553 K[a]
T_{si}	Sheath inside surface temperature	590 K[a]
F	Sheath oxidation enhancement factor	49
σ_g	Ratio of inner sheath surface area to gap volume	100082 m^{-1}[a]
T_{fs}	Fuel surface temperature	656 K[a]
ρ_s	Fuel density (at 273 K)[b]	10.65 Mg m^{-3}

[a] Values depend on the gap radial thickness, fuel-element power, coolant temperature and defect size. A gap size of 10 μm is assumed for all cases.

[b] A constant density is employed in Eq. (17) where c_u replaces ρ_s since C_p is given in units of J mol^{-1} K^{-1}.

The coupled partial differential equations are subject to the given initial conditions and Neumann and Dirchelet boundary conditions shown in Fig. 2. The constants of the model are further summarized in Table 1. The surface area of cracks per unit volume of fuel (m^{-1}) (σ_f) and ratio of the crack volume-to-solid fuel volume (ε) can be estimated in Appendix B. The sensitivity of the model to the various parameters is given in Section 4.1.

These equations are numerically solved with a finite-element technique using the FEMLAB (Version 3.1) software platform. The numerical implementation is detailed in Ref. [59]. The results of the calculation are given in Section 3.

3. Experimental results and model prediction

Experimental data of the O/M ratio from pellet samples taken from ten defective irradiated fuel elements were used to assess the fuel oxidation model. Samples were obtained by cutting the pellets into $\sim$10 mm thick discs and obtaining a small core drill sample ($\sim$2 mm in diameter to a depth of 5 mm) at various radial positions. The O/M ratio was determined with a coulometric titration (CT) technique that measures the amount of oxygen released from a heated sample in a controlled reducing environment [16,72]. For most elements, the experimental data yielded a radial profile (i.e., at a few axial posi-

Table 2
Summary of defect elements

Element[a]	Peak element linear power (kW/m)	Burnup (MWh/kgU)	Estimated post-defect residence time (Days)	Approximate largest defect area (mm^2)
K31	26	82[b]	>10	13
K22	35	84[b]	>10	$\leqslant$1.5
A18	50	176[b]	<1	<1
X4	45	76[c]	77	35
X5	44	139[c]	126	8
M6	44	235[c]	545	1
M14a	44	163[c]	311	4
M14b	45	167[c]	109	1
M11	46	179[c]	97	12
M15	51	89[c]	165	>25

[a] All data for elements K31, K22 and A18 were taken from Ref. [73], while data for all other elements were taken from Ref. [74].
[b] Element burnup.
[c] Bundle-average burnup.

Table 3
Parameters assumed/calculated in the simulation of the defective elements

Element	Operating history/calculated temperatures							Model input parameters	
	Linear power (kW/m)	PDRT[b] (d)	Bulk coolant temperature (K)	Fuel element temperatures (K)				Coolant Flow Direction[a]	Bulk gap flow (m/s)
				Sheath inside	Gap average	Fuel surface	Centre (Maximum)		
K31	26	38	550	584	615	645	1164	NRE → RE	0.0422
K22	34	62	553	597	638	679	1387	RE → NRE	1e−5
A18	50	0.25	533	602	673	743	2004	NRE → RE	1e−5
X4	43	77	573	629	680	732	1816	RE → NRE	1e−5
X5	41	126	553	606	656	706	1879	NRE → RE	1e−5
M6	41/40	200/345	553	597/596	641/639	686/682	1584/1641	RE → NRE	1e−5
M14a	42/36	178/133	553	598/592	644/630	689/669	1652/1487	RE → NRE	1e−5
M14b	41	280	553	597	641	686	1905	RE → NRE	1e−5
M11	44/43/25	60/109/206	566	614/ 612/ 593	663/ 658/ 619	712/ 705/ 645	1745/ 1936/ 1490	RE → NRE	1e−5
M15	44/51	98/8	553	600/ 608	648/ 664	696/ 719	1848/ 2123	NRE → RE	1e−5

[a] NRE: Non-reference end/RE: reference end.
[b] PDRT: Post-defect residence time estimated from data.

tions) for the O/M ratio. Optical microscopy was also used to assess the defect geometry, grain growth, and the presence of higher oxides. A summary of the case elements measured at the CRL is presented in Table 2 [73,74]. Information provided in Table 2 includes the element identity, element linear power and burnup, post-defect residence time (PDRT) for the defective element and (largest) defect area. A summary of the input model parameters is shown in Table 3, including the linear element power, post-defect residence time (PDRT) and bulk coolant temperature. The coolant flow direction is based on station data or observations of fission-product staining in the post-irradiation examination (PIE). A constant bulk-flow velocity was used for the higher-powered elements since the gap poses the largest restriction in flow as a result of fuel expansion. The calculated fuel centerline temperature is also shown in Table 3, where no centerline melting is predicted for any of the fuel elements over the linear power range of 26–51 kW/m.

Table 4 details the location and size of the defect(s) used in the model as estimated from the PIE for the ten elements. For those cases where an end cap was found to be leaking/defective, a small axial defect at that end of the element was assumed for the model simulation (which corresponds to a ring around the element for the two-dimensional representation). The axial coordinate begins at the non-reference end of the fuel stack ($z = 0$) and extends to $z = 0.484$ m for the standard 37-element bundle.

The measured oxygen-to-metal (O/M) profile data are used to assess the fuel oxidation kinetics model. The coulometric titration technique cannot distinguish the oxygen release from the UO_{2+x} matrix and the oxide phases in the fuel [13,60,75]. However, as shown in Table 5, the calculated oxygen-to-metal ratio for the UO_{2+x} solid phase, noble metal inclusions and solid phases (e.g., Cs_2ZrO_3 and UPd_3) changes only slightly with increased burnup for the typical H_2/H_2O ratios predicted by the fuel oxidation kinetics model (compare Fig. A.4 with Figs. A.3 and 21) [55]. Hence, as the degree of oxygen binding to the fuel is minor for typical CANDU fuel burnups, the O/M ratios measured at the CRL will be only slightly conservative compared to the O/U ratios of the fuel.

Figs. 3–12 show a comparison of the O/U predicted profiles and measured axial and radial O/M profiles for the elements. Representative model predictions of the deuterium mole fraction, fuel temperature and O/U profile are also shown in Fig. 13 for

Table 4
Simulated defect location and size for the defective elements

Element	Defect #1 axial location (m)	Defect #1 length (mm)	Defect #2 axial location (m)	Defect #2 length (mm)	Defect #3 axial location (m)	Defect #3 length (mm)	Defect #4 axial location (m)	Defect #4 length (mm)
K31	0.0	1.5	0.405	70.0	–	–	–	–
K22	0.205	0.5	0.48195	0.05	–		–	–
A18	0.025	0.5	0.4425	0.5	0.4675	0.5	–	–
X4	0.0365	2.5	0.2565	2.5	0.493	1.0	–	–
X5	0.0	1.0	0.259	4.0	0.490	4.0	–	–
M6	0.0	1.0	0.26	0.1	0.481	1.0	–	–
M14a	0.0	1.0	0.42	1.5	–	–	–	–
M14b	0.0	1.0	0.248	3.0	0.481	1.0	–	–
M11	0.0195	2.0	0.0434	4.0	0.128	36	0.474	2.0
M15	0.0195	0.5	0.075	0.5	0.145	51	–	–

Table 5
Oxygen-to-metal ratios as a function of added steam content for various burnups at a temperature of 1600 K

H_2O added (moles)	Burnup (MWh $(kgU)^{-1}$)				
	35	70	105	140	175
0	2.0057	2.0112	2.0163	2.0212	2.0259
0.1	2.0049	2.0091	2.0128	2.0163	2.0198
1	2.0064	2.0104	2.0142	2.0177	2.0211
10	2.0106	2.0144	2.0179	2.0212	2.0243
100	2.0237	2.0255	2.0271	2.0285	2.0299

* Based on the analysis in Ref. [55].

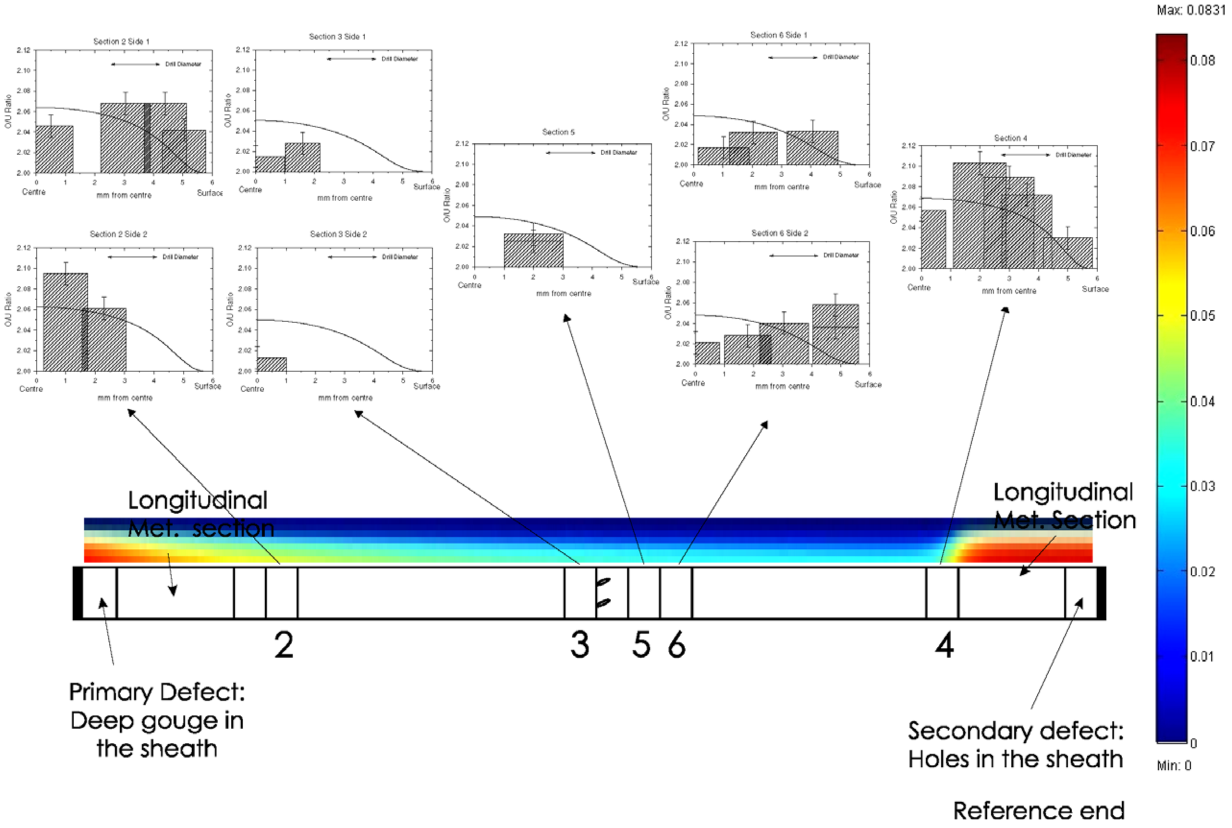

Fig. 3. Model predictions and O/M measurements for element K31.

element X5 as a radial cross-section plot under open blisters near the element mid-plane ($z = 0.260$ m), and as an axial cross-section plot at the fuel centerline ($r = 0$).

The model has also been expanded to a three-dimensional representation to account for the asymmetry of the defect geometry and azimuthal heat and mass transport [59]. This analysis shows that comparable results are obtained between the two and three-dimensional treatments for the temperature distribution for defective element X5 (Fig. 14). On the other hand, a one-dimensional analysis will over predict both the fuel oxidation and centreline temperature since this latter representation cannot account for the dispersion of heat or interstitial oxygen away from the defect site in the axial direction.

4. Discussion

The model is able to predict the extent and distribution of oxidation in defective fuel, as compared with O/M measurements made for research and commercial reactor defective elements. The predicted ratios peak towards the center of the pellet as a result of the Soret effect. The deviation from stoichiometry is greater near breaches in the sheath and increases with the size of defect (i.e., with a greater oxygen partial pressure). Oxidation decreases away from the defect site where hydrogen liberated from the sheath and fuel oxidation reactions builds up. As shown in Fig. A.3, a small hydrogen partial pressure can significantly reduce the fuel oxidation reaction. The fuel temperature also increases where the fuel oxidation is maximum, which is consistent with a decrease in the UO_2 thermal conductivity.

4.1. Sensitivity analysis

The current simulations indicate that the model is sensitive to defect size, post defect residence time (PDRT) and fuel linear heat rating. To investigate these effects, a sensitivity analysis was performed for defect element X5 since: (i) the observed defects were representative of failures seen in commercial

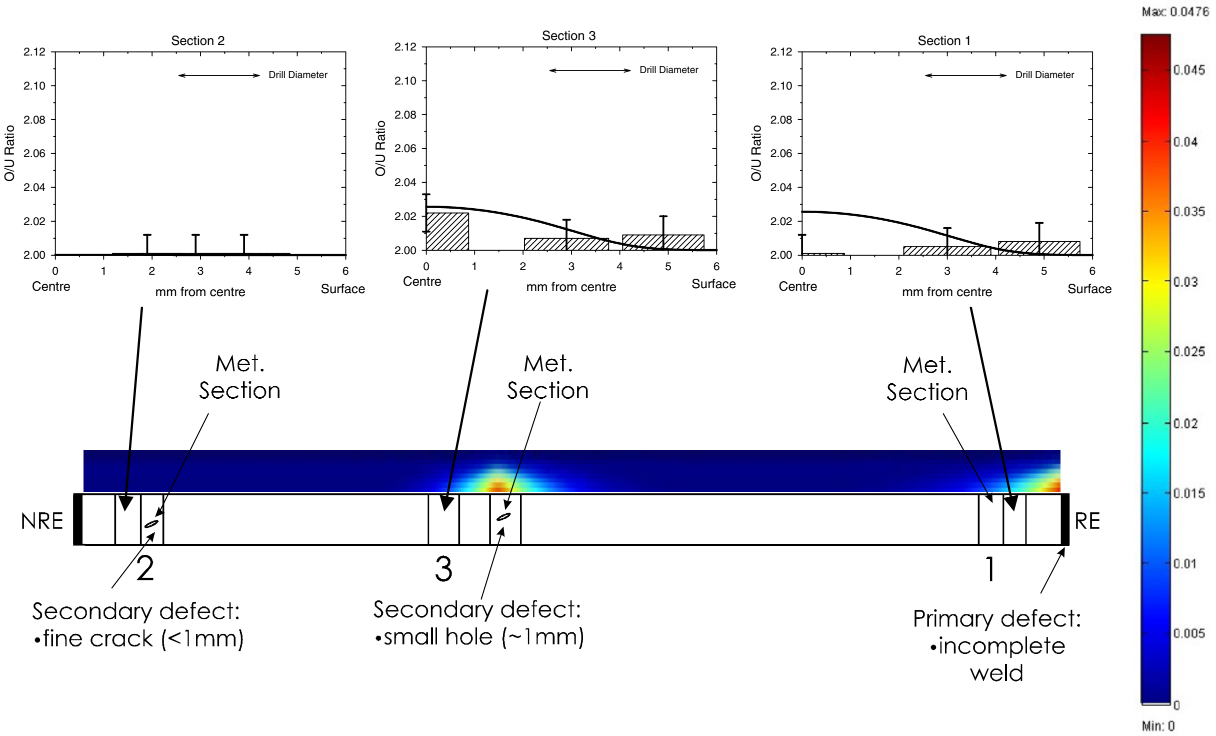

Fig. 4. Model predictions and O/M measurements for element K22.

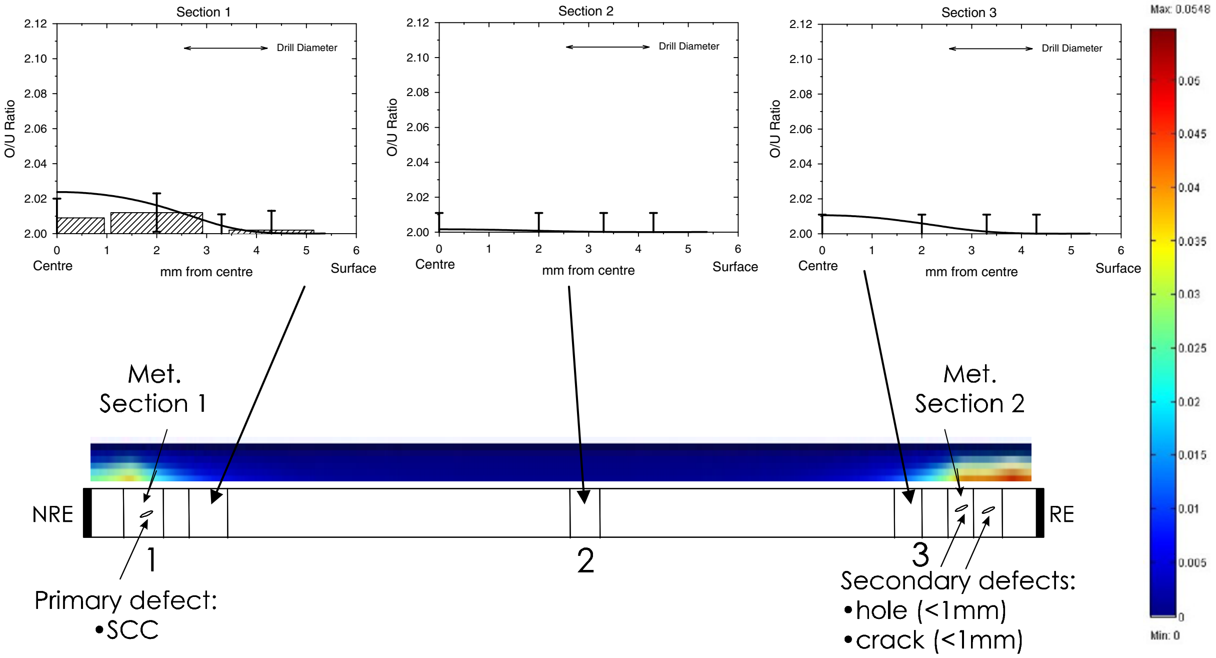

Fig. 5. Model predictions and O/M measurements for NRU element A18.

reactor operation; (ii) the linear operating power of this element is relatively high at 41 kW m^{-1}; and (iii) the post irradiation examination confirmed that the element had undergone significant oxidation and

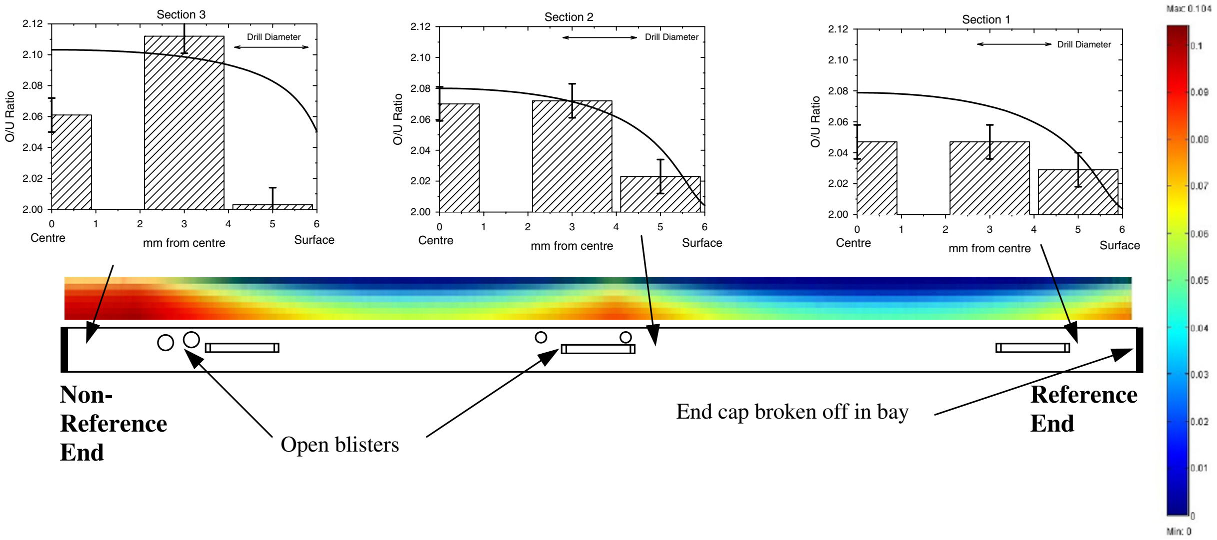

Fig. 6. Model predictions and O/M measurements for element X4.

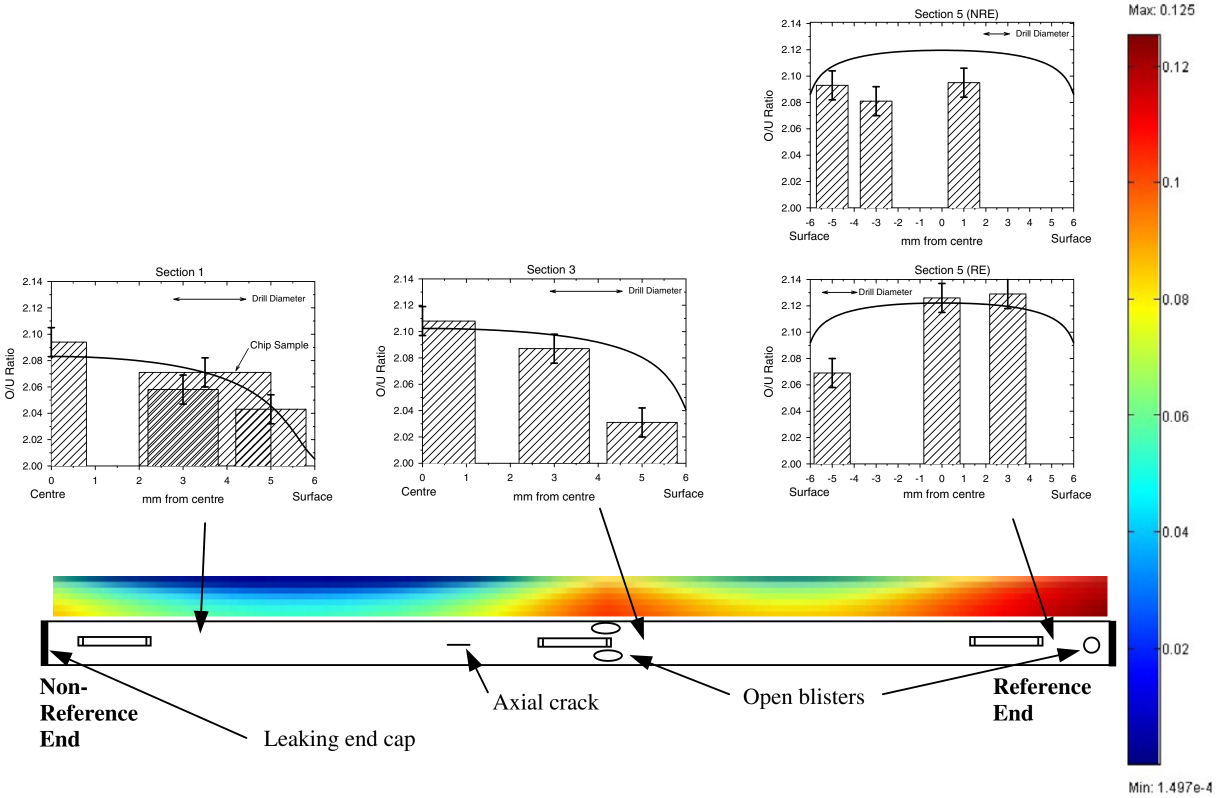

Fig. 7. Model predictions and O/M measurements for element X5.

fuel restructuring. Fig. 15 shows the maximum temperature and the stoichiometric deviation as a function of PDRT for various linear powers, where the amount of fuel oxidation and temperature are both

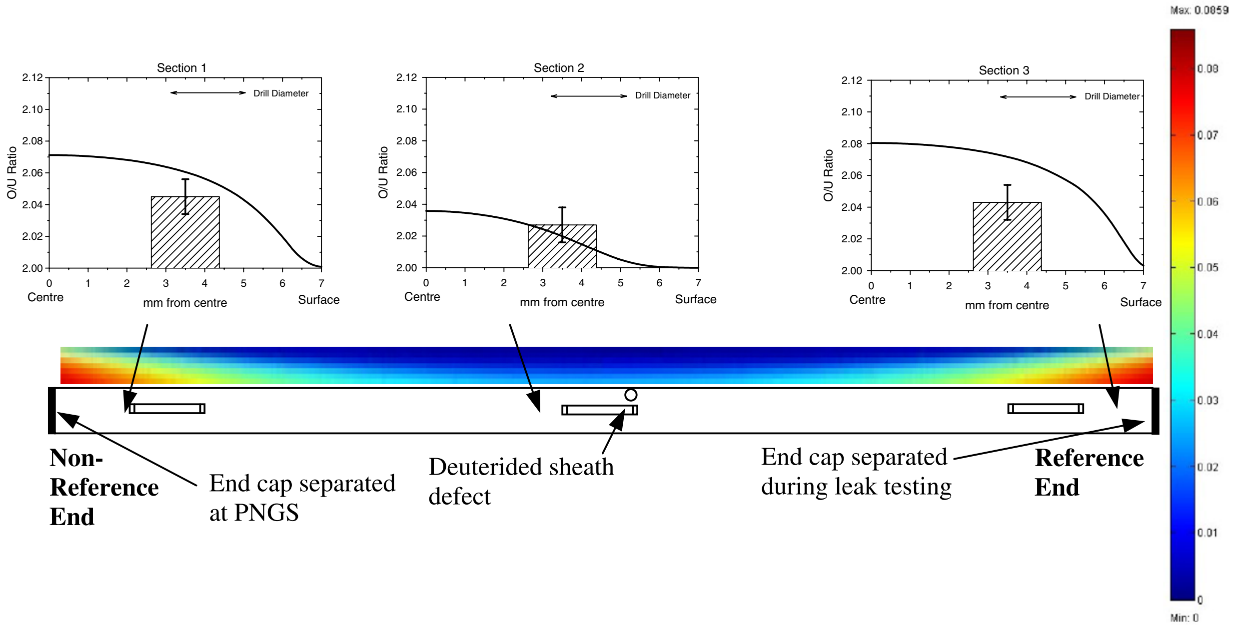

Fig. 8. Model predictions and O/M measurements for element M6.

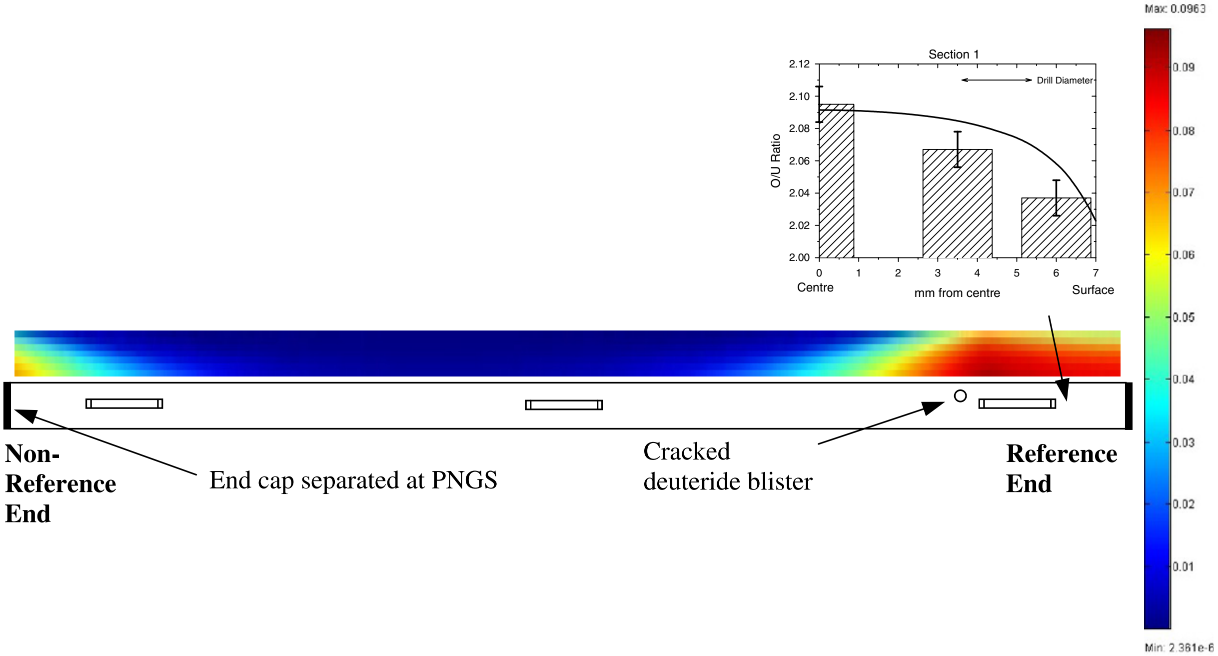

Fig. 9. Model predictions and O/M measurements for element M14a.

seen to increase with linear power. The model was also run for a post-defect simulation of 50 d for a variety of defect sizes as shown in Fig. 16.

The parameter ε in Eq. (42) of Appendix A depends on the number of fuel cracks and the location of the plastic core. Since these latter phenomena depend on element power (but in opposite directions), ε is relatively independent of the element power. The crack surface area-to-fuel volume ratio, σ_f, affects the fuel oxidation reaction kinetics as

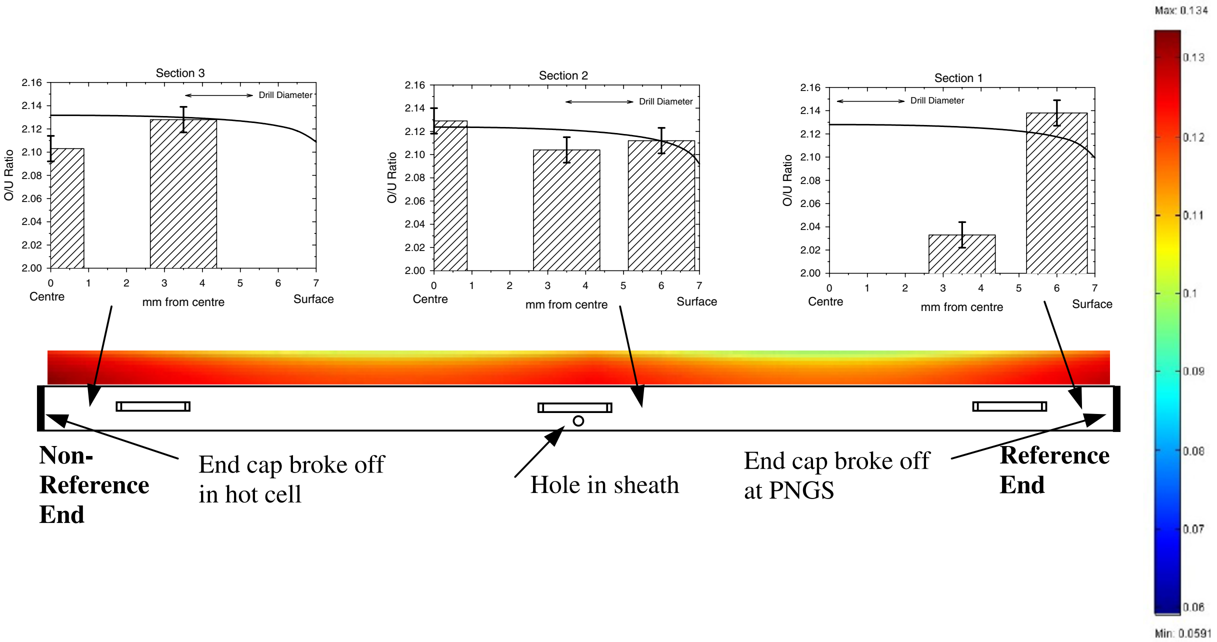

Fig. 10. Model predictions and O/M measurements for element M14b.

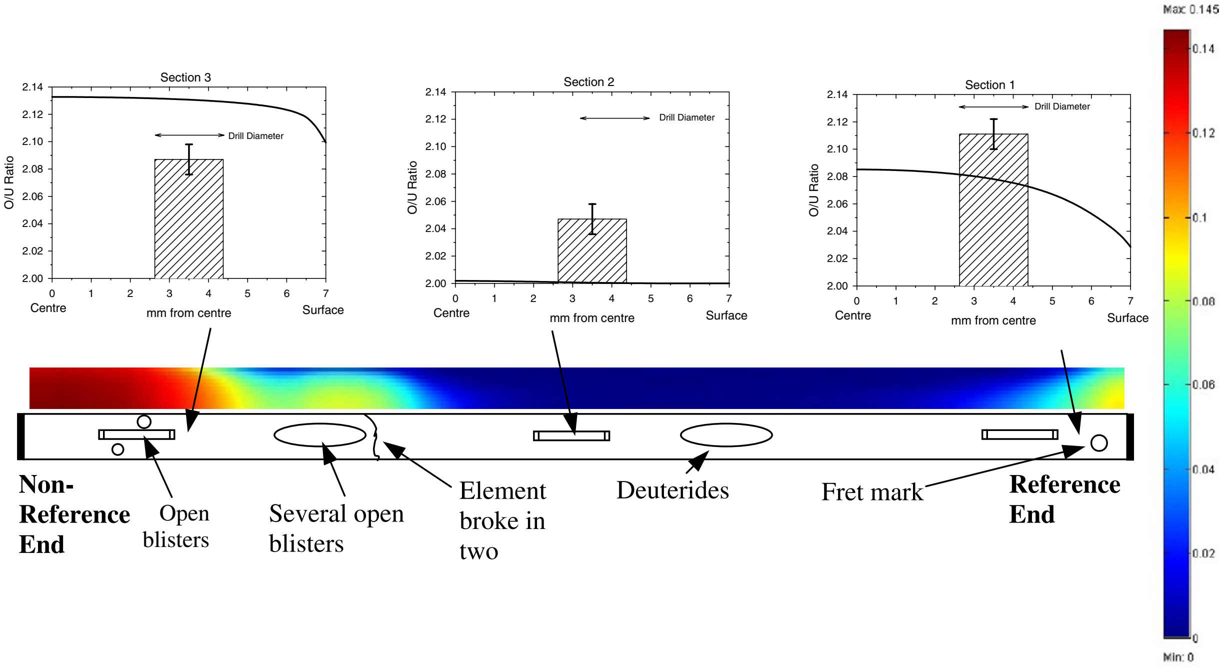

Fig. 11. Model predictions and O/M measurements for element M11.

applied in Eqs. (13) and (15). However, Fig. 17 shows little sensitivity when this parameter is reduced by a factor of two. This result indicates that under normal conditions (i.e., with a typical residence time of weeks to months), the oxidation kinetics are not significantly influenced by this parameter since there is sufficient time to reach an equilibrium condition of the stoichiometry deviation.

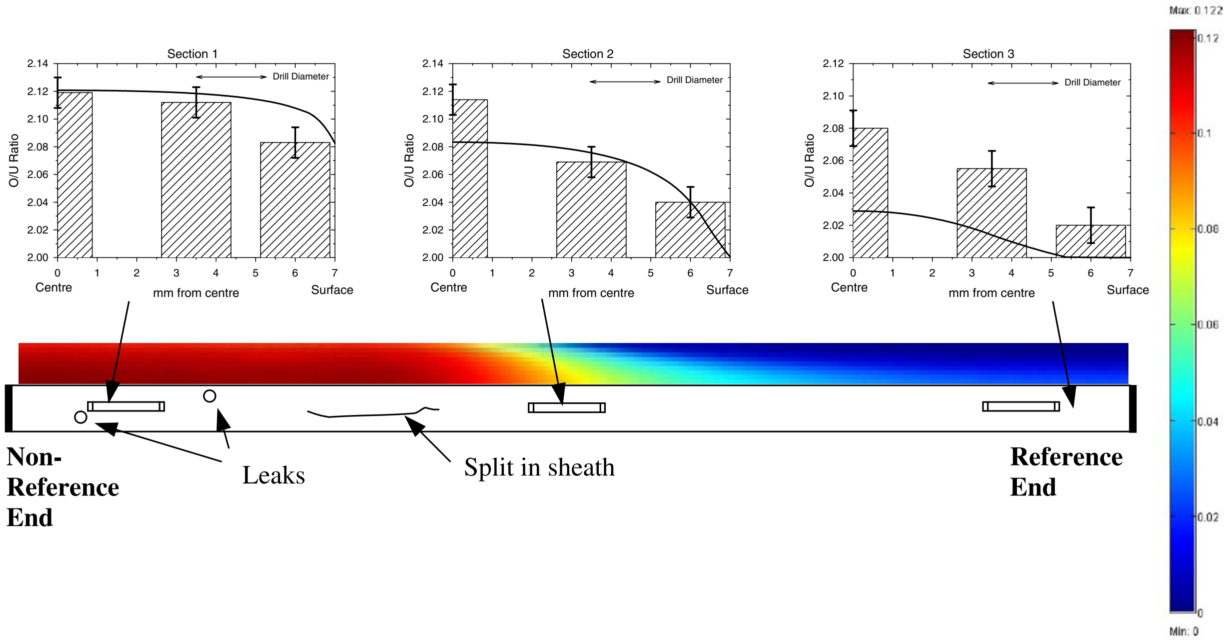

Fig. 12. Model predictions and O/M measurements for element M15.

The sensitivity of the model to the chemical diffusion coefficient is shown in Fig. 18. An enhanced diffusivity results in a flatter axial profile in Fig. 18(a) but a similar radial shape in Fig. 18(b) (which is dictated largely by the thermodynamics as a result of the large radial-temperature gradient). The chemical diffusion coefficient proposed in Eq. (10) is for annealing conditions. However, Matzke has proposed an enhancement in metal diffusion in UO_2 with the fission rate, particularly at low temperatures (<1000 °C) [33]. On the other hand, since the chemical diffusion of oxygen in uranium dioxide is many orders of magnitude greater than metal diffusion, the effect of irradiation enhancement of oxygen diffusion is not expected to be significant.

The kinetics model in Eq. (9) only strictly applies to fuel oxidation (i.e., where locally $x < x_e$ so that $R_f^{\text{react}} > 0$). However, as a result of gas phase transport of hydrogen in the fuel cracks, fuel reduction can also occur (where $R_f^{\text{react}} < 0$). To account for this possibility, it is conservatively assumed in the current treatment that fuel reduction occurs at the same rate as fuel oxidation (when $x > x_e$). In this analysis, the factor $(1 - q)$ in the reaction rate term of Eq. (9) is replaced by q so that the fuel reduction kinetics depends instead on the hydrogen partial pressure. However, limited annealing experiments under reducing conditions indicate that the fuel reduction reaction is much more rapid by several orders of magnitude [30]. Thus, the sensitivity of the model to the fuel-reduction reaction rate was further investigated by increasing R_f^{red}in Eq. (9) by factors of 10 and 100. As shown in Fig. 19, the maximum temperature and stoichiometric deviation are reduced by only ~10%. This relative insensitivity arises because the fuel reduction reaction primarily occurs in a small region near the periphery of the pellet where the fuel temperatures are low (see Fig. 20).

4.2. Thermal diffusion of H_2 in cracks

Since the gases in the fuel cracks are assumed to be at the same temperature as the fuel, thermal diffusion may also impact hydrogen transport in the fuel cracks. The importance of thermal diffusion can be characterized by a 'thermal diffusion ratio' [17]:

$$k_T = \frac{\rho}{c^2 M_A M_B} \frac{D_A^T}{D_{AB}}, \tag{30}$$

where ρ is the mass density and c the molar density of the gas mixture, M_A and M_B are the molecular weight of species A and B, respectively, D_A^T is the thermal diffusion coefficient for species A, and D_{AB} the ordinary binary diffusion coefficient. The flux of species A in a binary mixture is:

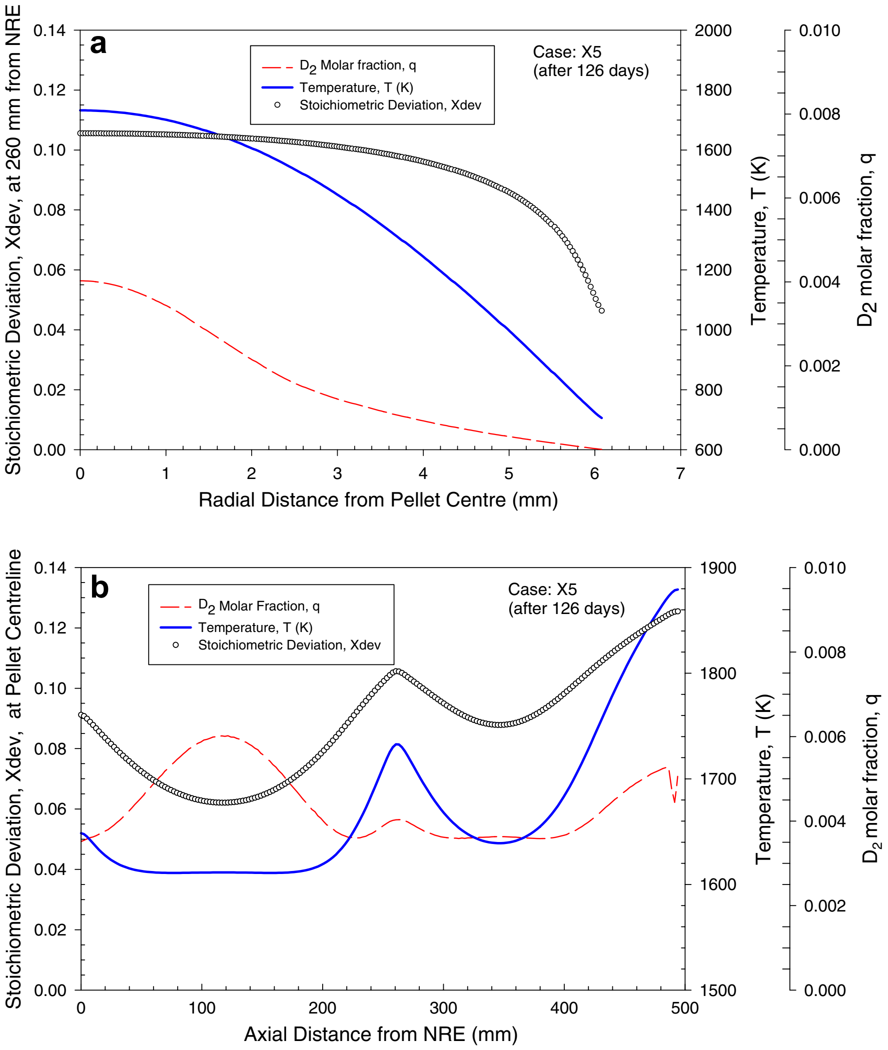

Fig. 13. Model predictions of deuterium mole fraction, stoichiometry deviation and fuel temperature for element X5. (a) Radial profile under open blisters at the element axial midplane and (b) axial profile at the fuel centerline.

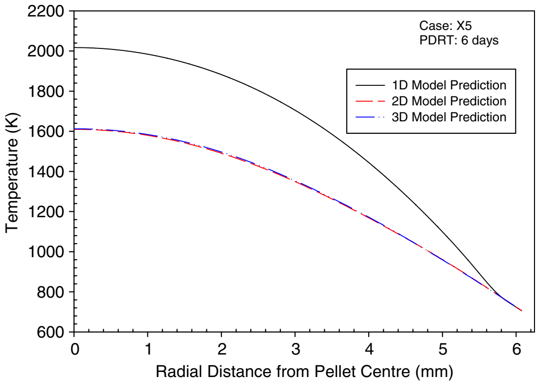

Fig. 14. Comparison of 1-D, 2-D, and 3-D model predictions for temperature for a PDRT of 6 d.

$$j_A = -j_B = \left(\frac{c^2}{\rho}\right) M_A M_B D_{AB} [\nabla x_A + k_T \nabla \ln T], \tag{31}$$

where x_A is the mole fraction of species A. Thus, the equation for hydrogen transport within the fuel cracks in Eq. (15) can be modified as such:

$$\varepsilon c_g \frac{\partial q}{\partial t} = \frac{\varepsilon}{\tau^2 r}\left[\frac{\partial}{\partial r}\left(r c_g D_g \left(\frac{\partial q}{\partial r} + \frac{k_T}{T c_g}\frac{\partial T}{\partial r}\right)\right)\right] + \sigma_f R_f^{\text{react}}. \tag{32}$$

Using the correlation of Kihara for binary mixtures [76], and assuming a hydrogen mole fraction of 0.005, the thermal diffusion ratio for hydrogen in

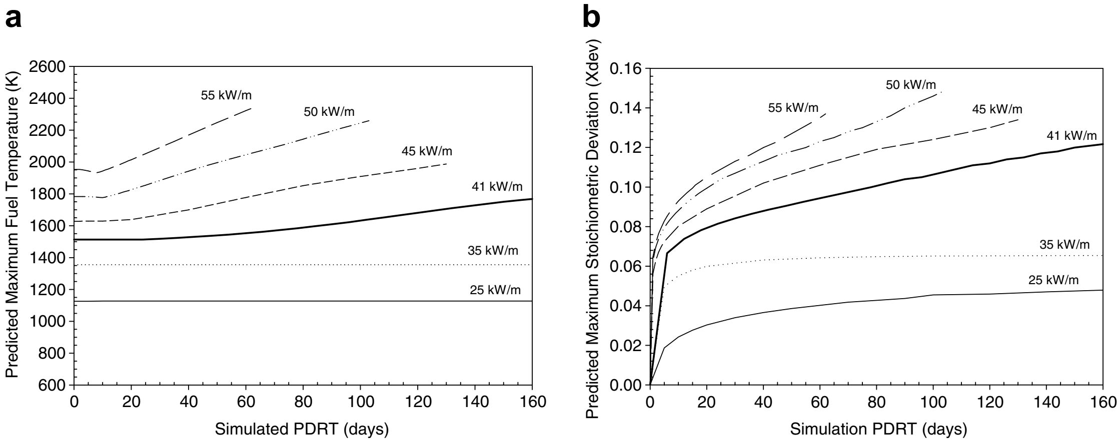

Fig. 15. Model predictions of (a) maximum fuel temperature and (b) maximum stoichiometry deviation versus linear power for element X5.

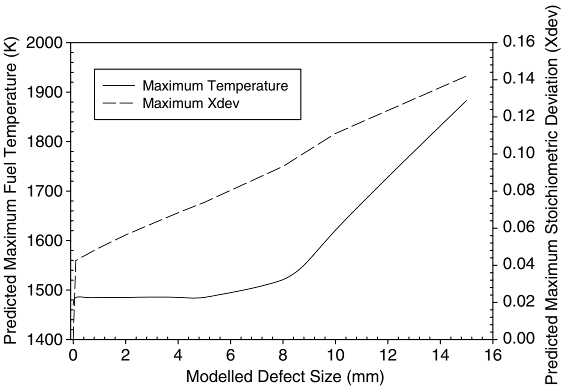

Fig. 16. Model predictions of maximum fuel temperature and maximum stoichiometry deviation as a function of defect size.

a hydrogen-steam mixture is evaluated as a function of temperature T (K) as [59]:

$$k_T = 2.47 \times 10^{-4} + 9.3 \times 10^{-7} T \tag{33}$$

Thus, using Eqs. (32) and (33), the relative effect of normal versus thermal diffusion can be evaluated. Since the magnitude of the thermal diffusive flux $D_g\left(\frac{k_T}{Tc_g}\frac{\partial T}{\partial r}\right)$ is calculated to be less than 0.1% of the normal diffusive flux $D_g\left(\frac{\partial q}{\partial r}\right)$ over the pellet radius for case X5, thermal diffusion can be neglected in the fuel cracks.

The Soret effect results in a greater migration of interstitial oxygen to the centre of the pellet. In addition to this mass transfer in a temperature gradient, the Dufour effect will also arise as a coupled

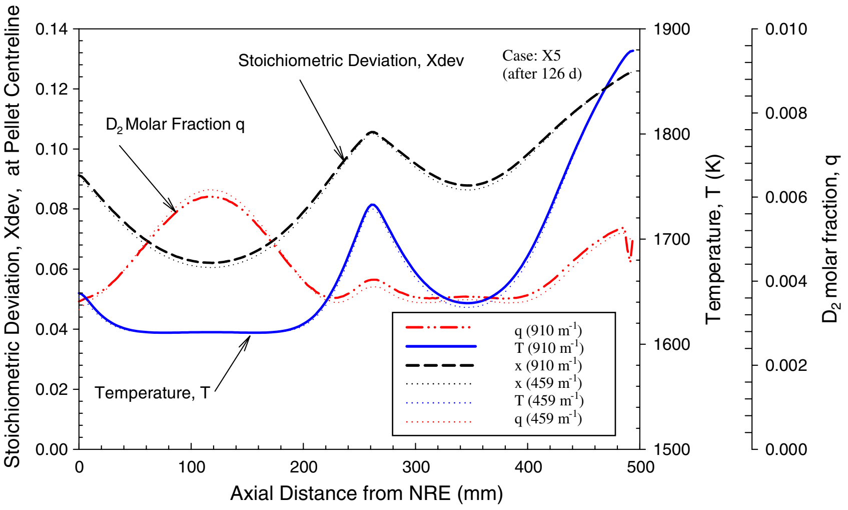

Fig. 17. Model sensitivity to the parameter σ_f (as shown in brackets in the legend).

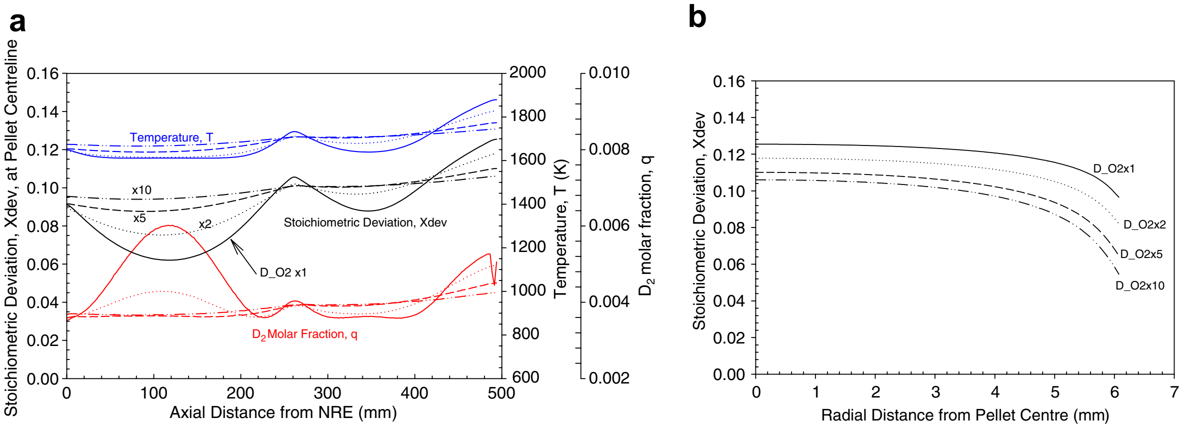

Fig. 18. Model sensitivity to the oxygen chemical diffusion coefficient for Case X5 (after 126 d) showing an (a) axial slice at the pellet centerline and (b) radial slice through the largest defect at the reference end.

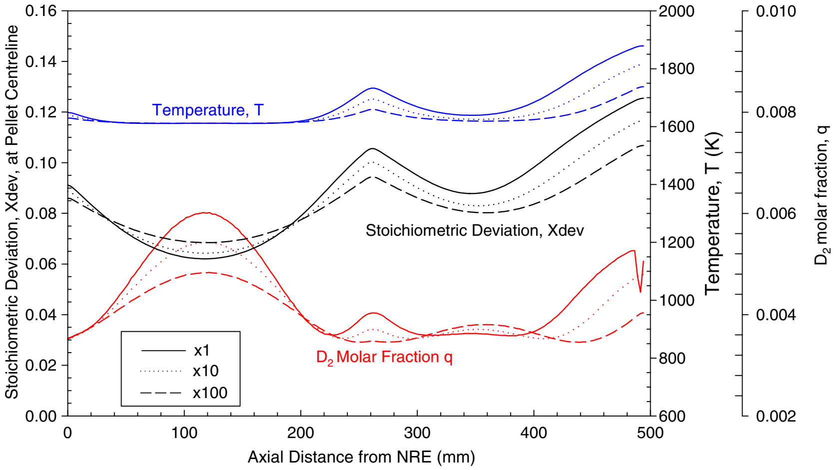

Fig. 19. Model sensitivity to fuel reduction reaction rate for Case X5 (after 126 d).

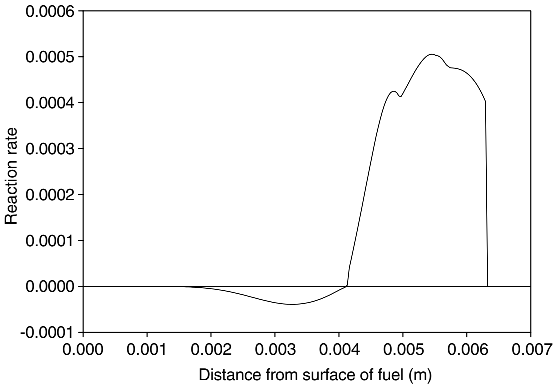

Fig. 20. Plot of the fuel oxidation and reduction reaction rate (in mol H_2 or O m^{-2} s^{-1}) for a radial slice under the largest defect of element X5.

effect where there is an energy flux associated with the mass transfer [77]. However, this effect is neglected in this treatment since this amount of heat is small in comparison to the heat generated in the fission process.

4.3. *Effect of low-temperature reactor operation and out-reactor effects on the fuel oxidation behaviour*

The presence of oxides higher than UO_{2+x} are often observed in the PIE of defective fuel (Fig. 22). Enhanced oxidation kinetics may occur from coolant radiolysis (Section 4.3.1). In addition, if the fuel cooldown is not too fast, higher-oxide

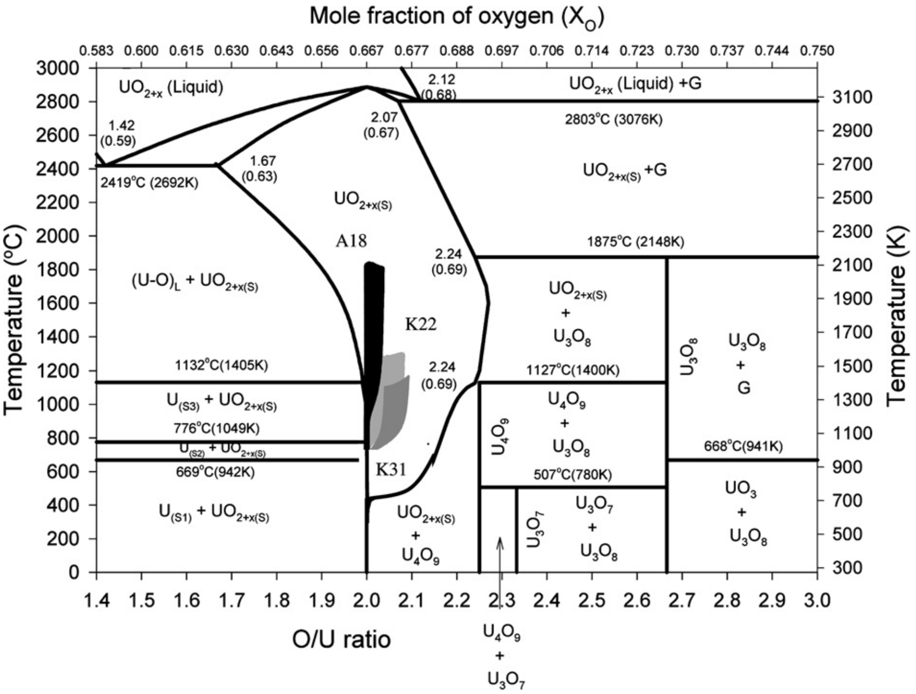

Fig. 21. Temperature versus O/U ratio space for the three defective elements as plotted on the U–O phase diagram.

phases could also arise during reactor shutdown as a result of U_4O_9 precipitation (Section 4.3.2) [78]. In addition, continued fuel oxidation can also result from out-reactor effects (Section 4.3.3). It is important to assess these post-irradiation effects since the O/M profile data in Section 3 used for the validation of the in-reactor fuel oxidation model also encompass these out-reactor phenomena.

4.3.1. Radiolysis effects

Grain-boundary oxidation has been observed in defective fuel under the defect site(s) and in the fuel crack regions of defective elements (Fig. 22). Steam oxidation to higher oxide phases is precluded on thermodynamic grounds with the presence of hydrogen (see Fig. A.3). However, fuel oxidation could be enhanced by coolant radiolysis with the formation of the highly-reactive hydrogen peroxide species. In fact, it has been suggested that this reactive metastable species can equilibrate with the fuel and oxidize it even in the presence of hydrogen [79]. However, hydrogen liberated in the H_2O_2 oxidation reaction could also neutralize the tendency of the oxidizing counterparts to increase the stoichiometry of the fuel [5]. Energy-deposition calculations also suggest that radiolysis does not substantially enhance the fuel oxidation kinetics at high pressure in operating defective elements [6]. At higher temperatures, radiolytic effects should become insignificant in comparison to thermal effects as the thermal reactions and the recombination of transient species become faster. It is therefore expected that any radiolysis-enhanced oxidation would be limited and localized at or near the fuel surface and close to the defect site.

4.3.2. U_4O_{9-y} non-stoichiometry and U_4O_9 precipitation from UO_{2+x}

The thermodynamic treatment in Fig. A.1 is in agreement with a large body of experimental data. The calculated U–O phase diagram, as well as a recent evaluation of this system [51], take the U_4O_9 phase to be stoichiometric as a reasonable approximation. Many investigators, however, have shown that U_4O_9 is a narrowly non-stoichiometric phase (U_4O_{9-y}). Experiments have shown that three phases exist: α-U_4O_{9-y} (below ~80 °C), β-U_4O_{9-y} (between ~80 °C and ~550 °C) and γ-U_4O_{9-y} (above ~550 °C) [80]. Fig. 23 shows a summary of the experimental data on the location of the phase boundaries for U_4O_{9-y} as well as the proposed fields for the three phases of U_4O_{9-y} [38–43,45–50,81,82].

To gain a better understanding of the U_4O_9 non-stoichiometry, an *in situ* neutron diffraction experiment was further performed at the Los Alamos

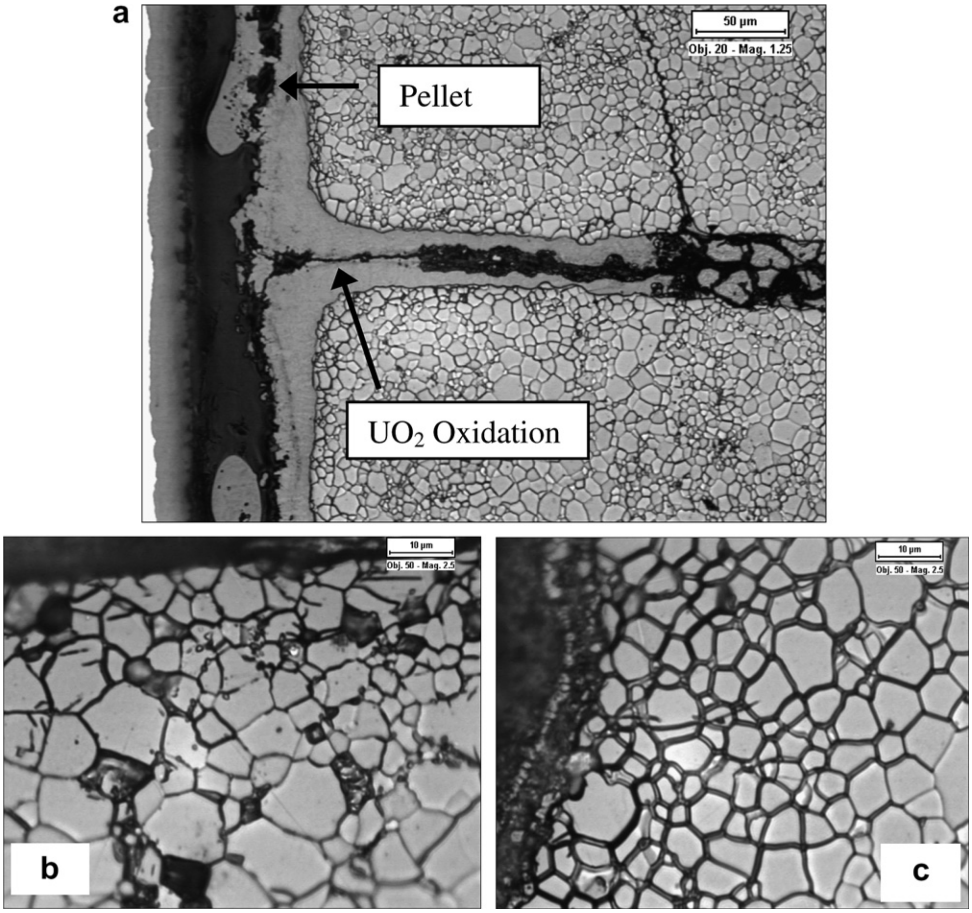

Fig. 22. (a) UO_2 oxidation (gray areas) near the primary defect of K31. Grain boundary oxidation in (a) is shown in the magnified figures: (b) along the fuel pellet surface and (c) near a radial fuel crack.

Neutron Science Center (LANSCE) in this work [83,84]. Details of this experiment is given in Refs. [59,85]. Here depleted UO_{2+x} powder was heated from room temperature to a maximum of 1150 °C while exposed to a neutron beam inside a time-of-flight neutron diffraction instrument. Rietveld refinement of the diffraction patterns provided a measure of the weight fraction and respective lattice parameters. The best fit to the data was obtained using the UO_2 space group Fm3m from Hutchings [86] and the $UO_{2.234}$ space group I43d from Kim et al. [87]. The latter phase could also be expressed as $U_4O_{8.936}$, (or U_4O_{9-y}, where y is 0.064), which provides further evidence that U_4O_9 has a non-stoichiometric field at elevated temperature [88]. Although the U_4O_9 phase is slightly hypo-stoichiometric, this observation will not significantly affect the thermodynamic analysis in Appendix A.

The precipitation kinetics of U_4O_9 from UO_{2+x} was also investigated in the LANSCE experiment. If the UO_{2+x} is rapidly quenched from high temperatures, a single phase UO_{2+x} can be 'frozen in' when there is little time for diffusion or other processes of structural rearrangement of ions to take place [82]. However, the U_4O_{9-y} was observed to precipitate out of the UO_{2+x} at a relatively low temperature (200–400 °C), where this system approached thermodynamic phase equilibrium in less than one hour [59,85]. The values of the UO_2 and $UO_{2.234}$ lattice parameters in this study compared well with published values (Fig. 24) [38,61,80,87]. Although the current experimental setup (maximum cooling rate of 0.3 °C s^{-1}) was unable to simulate rapid cool-down operations, one cannot rule out the possibility that the U_4O_9 observed in the PIE examination at the CRL may be due to precipitation of the UO_{2+x}.

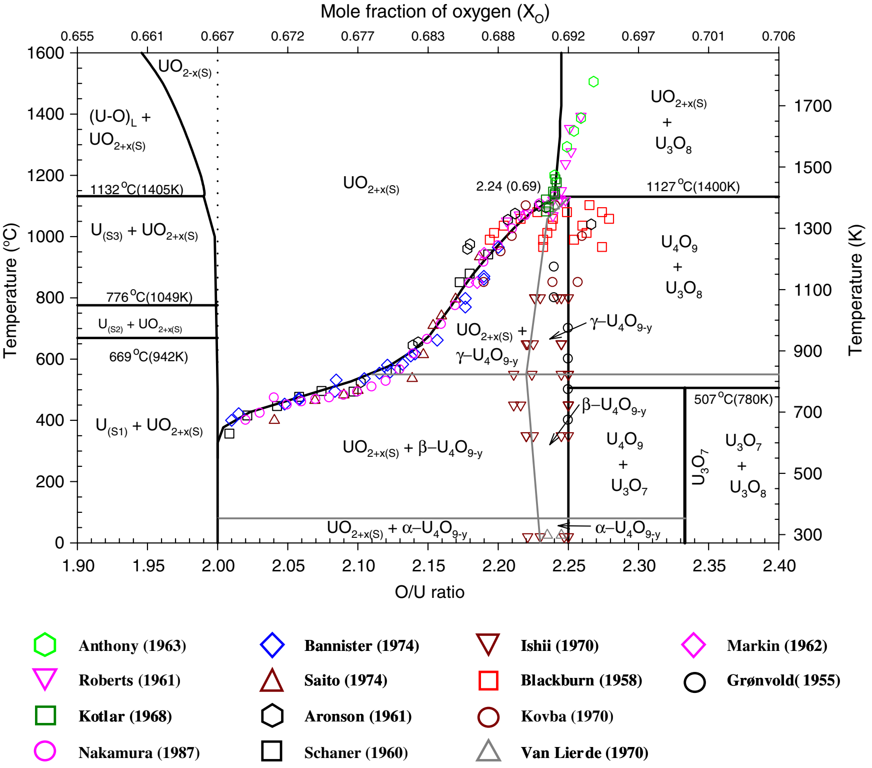

*The horizontal line constructions (grey) at 80°C and 550°C reflect the inability to distinguish the transformation temperatures in the adjacent two-phase fields.

Fig. 23. Calculated U–O phase diagram in area of interest compared with experimental data.

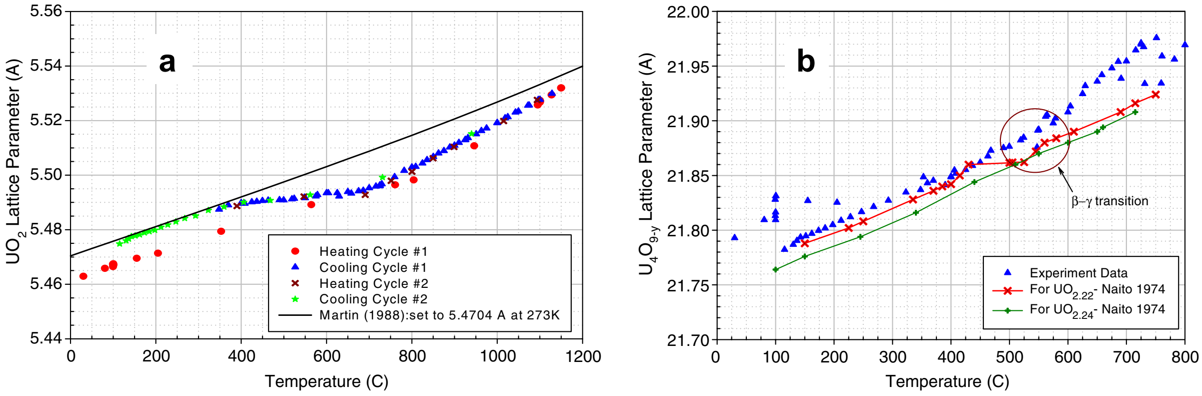

Fig. 24. Calculated lattice parameters at various temperatures for the (a) UO_2 and (b) U_4O_{9-y} phases. Data are taken from Refs. [61,80].

4.3.3. Out-reactor effects

Fuel oxidation can also occur post-irradiation from: (i) fuel transfer operations where, for instance, moist air is present during fuel discharge from the refueling machine and (ii) long-term storage of defective fuel in the fuel bays in which there is dissolved oxygen in the bay water.

4.3.4. Low-temperature oxidation effects in air (fuel transfer operation)

The air oxidation of UO_2 proceeds via a two-step reaction [89]:

$$UO_2 \rightarrow U_4O_9/U_3O_7 \rightarrow U_3O_8. \quad (34)$$

This process has been studied because of its importance to dry storage and disposal of used nuclear fuel [90–102].

The 'intermediate' phase(s), U_4O_9/U_3O_7, forms as a discrete layer of thickness X on the surface of the UO_2 sample that thickens with time. Since the reaction rate is limited by oxygen diffusion through the surface layer, it can be modeled as a moving-boundary problem [90,91,97]:

$$X = a\xi\lfloor 1-(1-C)^{1/3}\rfloor = \sqrt{kt} \tag{35}$$

Here $\xi \sim 0.99$ is the ratio of the molar volume of U_4O_9/U_3O_7 to that of UO_2 and C is the fraction of UO_2 converted to U_4O_9/U_3O_7. The parameter k ($\mathrm{m^2\,s^{-1}}$) is a parabolic rate constant developed from experimental data [103]

$$\ln k = -\frac{95.7\mathrm{kJ\ mol^{-1}}}{R}T - 17.33, \tag{36}$$

where $R = 8.314 \times 10^{-3}\ \mathrm{kJ\ K^{-1}\ mol^{-1}}$ is the ideal gas constant and T is the temperature (K).

The discharge of irradiated fuel into the fuel discharge mechanism at one of the CANDU stations requires that fuel be raised above the water level and moved in air in the irradiated fuel port until it is lowered into the fuel bay. Here the transfer time in air is ~225 s. As a sample calculation, consider the transfer of a defective fuel bundle, where it experiences an air environment for $t = 225$ s at ~373 K. In this case, assuming a typical grain radius of $a_g = 5\ \mu\mathrm{m}$, Eqs. (35) and (36) yield a product layer thickness of $X \sim 5 \times 10^{-4}\ \mu\mathrm{m}$, with a negligible fraction of UO_2 converted into U_4O_9/U_3O_7 of $C \sim 3.1 \times 10^{-2}\%$. This analysis, therefore, suggests that U_4O_9/U_3O_7 formation is negligible during normal refueling operations.

For the second step in the reaction of Eq. (34), a conservative estimate can be made by assuming that grain-boundary diffusion is relatively rapid compared to the rate of U_3O_8 formation since the three-dimensional bulk formation of U_3O_8 will be slower than unhindered oxidation along the surface [103]. This conservatism though may be reduced by enhancement effects due to the production of nitrogen oxides formed by radiolysis of air [103]. The sigmoidal reaction kinetics for the nucleation-and-growth mechanism for U_3O_8 formation is described by [103]:

$$\alpha = 1 - e^{-(\pi/3)\kappa t^3}, \tag{37}$$

where α is the fraction of material converted to U_3O_8 at time t. The reaction rate constant κ (in $\mathrm{h^{-3}}$) is derived as a function of temperature T (in K) from literature data [103]:

$$\ln\kappa = (-52808 \pm 3.442)/T + 86.165. \tag{38}$$

Thus, for the given example for transfer of a defective fuel bundle, Eqs. (37) and (38) also predict a negligible fraction.

Hence, higher-oxide formation (post-shutdown) is not an important consideration during normal refueling operations because of the limited time in air and the low temperature, although this analysis has neglected the effect of moisture (i.e., relative humidity, RH) [104]. With irradiated fuel, water is also a potential source of radiolytic oxidation products; however, moisture has less of an effect on irradiated fuel samples (at RH $<$ 33%) [101]. At RH $<$ 40%, the mechanisms are the same as that for dry oxidation, yielding the bulk products shown in Eq. (34) [105]. In aerated water (i.e., RH $>$ 40%), mixtures of U_3O_8 and dehydrated schoepite (DS) have been observed [100,105–108]. High-moisture (100% RH) limited-air tests on irradiated CANDU fuel at 150 °C further suggest that moisture enhances the extent of grain boundary oxidation [109].

4.3.5. Low-temperature oxidation effects in water (fuel bay storage)

Spent defective fuel bundles are eventually stored for long periods of time (i.e., at least several years) in water bays at ~30 °C. The water bays are oxygenated since they are open to the air surface.

Experiments conducted in a closed autoclave with fresh CANDU fuel specimens, i.e., in aerated water for ~20 d at ~200 °C, have indicated that fuel oxidation can occur via: (i) solid-state diffusion to U_3O_7 (similar to dry oxidation as described above), (ii) oxidative dissolution and precipitation of U(VI) as $\sim(UO_3)\cdot 0.8H_2O$ and (iii) back-reduction of dissolved U(VI) on the UO_2/U_3O_7 surface to form U_3O_8 [107]. These species are also consistent with the computed Pourbaix diagram in Fig. A.5, which shows the dissolution/precipitation product of $UO_3(H_2O)$. The formation of U_3O_8 though from aqueous solutions is rarely reported [107]. Corrosion experiments with fragments taken from irradiated Boiling Water Reactor (BWR) fuel pellets ($\sim 34\ \mathrm{GWd\cdot(tU)^{-1}}$) that were conducted at 340 °C and 15 MPa for up to ~50 h indicated the occurrence of microcracks along the grain boundaries due to preferential U_4O_9 formation (i.e., in water with more than several ppm of dissolved oxygen) [110].

However, it would be expected that such out-reactor effects are small since defective elements K22 and A18 spent long periods in the fuel bays similar to K31 (see Section 3). Thus, the lack of fuel oxidation in defective elements K22 and A18 suggest that the contribution of out-reactor oxidation in K31 is small especially compared to in-reactor oxidation.

5. Conclusions

1. A theoretical treatment has been developed to describe the fuel oxidation behaviour in operating defective nuclear fuel elements. The model accounts for steam/hydrogen transport in the fuel-to-sheath gap for estimation of the hydrogen-to-steam partial pressure ratio in the gap. A thermodynamic treatment has been employed to calculate the equilibrium state of the oxidized fuel. The fuel oxidation kinetics model accounts for multi-phase transport including both normal diffusion and thermodiffusion for interstitial oxygen migration in the solid and gas-phase transport of hydrogen/steam in the fuel cracks. The fuel oxidation model is coupled to a heat conduction model to account for the feedback effect of a reduced thermal conductivity in hyperstoichiometric fuel. A numerical solution of the governing coupled equations has been obtained using a finite-element technique with the FEMLAB 3.1 software package.
2. A two-dimensional (azimuthally-symmetric) model has been developed to determine the radial and axial profile of the oxygen-to-uranium (O/U) ratio in the defective element. The model has been assessed against measured O/M profiles obtained with a coulometric titration method with very small samples taken from ten spent defective elements discharged from the NRU and commercial reactors.
3. The current theoretical analysis indicates that fuel oxidation is primarily dependent on defect size, post-defect residence time and fuel linear heat rating. Thermodynamics precludes the formation of oxides higher than UO_{2+x} in operating defective fuel elements (especially at higher temperatures and with hydrogen present); however, experiments at the Los Alamos National Laboratory suggest that U_4O_9 may have time to precipitate from UO_{2+x} on reactor cooldown or during bundle discharge and be observed as an artifact at room temperature. Assessment of the in-reactor model against the O/M measurements may also be complicated with the possibility of oxidation occurring out-reactor due to fuel transfer operations and long-term storage in fuel bays, although such effects are expected to be small.

Acknowledgements

The authors would like to acknowledge helpful discussions with M.R. Floyd, Dr Z. He and Dr R.A. Verrall on experimental O/M profile determination and ceramography examination, and to thank J. Judah of Ontario Power Generation for providing valuable post-irradiation examination data. The authors would also like to thank Dr S. Kupca (Director General of Nuclear Safety (DGNS)) for support of this work, and Professor D.R. Olander (UCB) for many helpful discussions on fuel oxidation modelling. In addition, the authors wish to express their thanks to Dr S. Vogel of the Los Alamos Neutron Science Centre (LANSCE) for collaboration on the kinetics of U_4O_9 precipitation. The authors would also like to acknowledge the assistance of Drs M. Kaye and F. Akbari at the RMC.

This work has benefited from the use of the Los Alamos Neutron Science Center at the Los Alamos National Laboratory. This facility is funded by the US Department of Energy under Contract W-7405-ENG-36. The current work was sponsored by the CANDU Owners Group (COG) under work package WP 22324, the Natural Sciences and Engineering Research Council (NSERC) of Canada (Collaborative Research Development grant and individual Discovery grants for both B.J. Lewis and W.T. Thompson) and the DGNS of the Department of National Defence.

Appendix A. Thermodynamic considerations

A thermodynamic model is required to determine the equilibrium state of the oxidized fuel (x_e) (Appendix A.1). The thermodynamic model can also be used to assess the aqueous species of uranium to better understand the out-reactor oxidation behaviour of defective fuel stored in water bays (Appendix A.2).

A.1. Fuel oxygen potential and the uranium–oxygen phase diagram

Following the methodology in Ref. [7], this work incorporates an improved thermodynamic treatment of the U–O system with emphasis on the location of the $UO_{2+x}-U_4O_9$ phase boundary, and the behaviour of p_{O_2} over the entire range of UO_{2+x} (652–3100 K) (see Fig. A.1) [34–50]:

$$\begin{aligned}\log p_{O_2} = {} & -11414.6 - 0.249T + 1.096\times10^{-5}T^2 \\ & + 3103.86\log T - 86170637T^{-1} \\ & + 3.118607\times10^{8}T^{-2} + 3545460(\log T)/T \\ & - 2\log((1-x)/x) + 1.832x + 32.15x^2 \\ & - 150.31x^3 + 503.02x^4. \qquad (39a)\end{aligned}$$

A similar expression is also available for the partial pressure of UO_3 (in atm) over solid UO_{2+x} (for 652–3100 K):

$$\begin{aligned}\log p_{UO_3} = {} & -6454.2 - 0.1437T + 5.482\times10^{-6}T^2 \\ & + 1771.5\log(T) - 4.17426\times10^{6}/T \\ & + 1.20993\times10^{8}/T^2 + 1.77273 \\ & \times 10^{6}\log(T)/T - \log((1-x)/x) \\ & + 0.9158x + 16.08x^2 - 75.15x^3 + 251.51x^4. \\ & \qquad (39b)\end{aligned}$$

Isobaric lines of oxygen and UO_3 partial pressure are depicted in the U–O phase diagram of Fig. A.2. Although the treatment in Fig. A.1 is true to the many solubility measurements of U_4O_9 in UO_{2+x}, there is a slight deviation from the data of Anthony et al. [45] from 1500 to 1900 K. This deviation was justified in order to be in reasonable agreement with the published thermodynamic values for U_3O_8. It should be noted that a recent treatment of the U–O system by Chevalier et al. deviates from the measurements in this region in a similar manner [51].

An expression relating the hydrogen-to-steam partial pressure ratio, temperature T (in K) and equilibrium stoichiometric deviation x_e follows from the thermodynamic analysis: For the (H_2/H_2O) variation of the UO_{2+x} non-stoichiometry:

$$\begin{aligned}\log\left(\frac{p_{H_2}}{p_{H_2O}}\right) = {} & 5706.8 + 0.1245T - 5.482\times10^{-6}T^2 \\ & + \frac{4296016}{T} - 1550.95\log(T) \\ & - \frac{1772730\log(T)}{T} - \frac{155930359}{T^2} \\ & + \log\left(\frac{1-x_e}{x_e}\right) - 0.9158x_e - 16.076x_e^2 \\ & + 75.154x_e^3 - 251.51x_e^4. \qquad (40)\end{aligned}$$

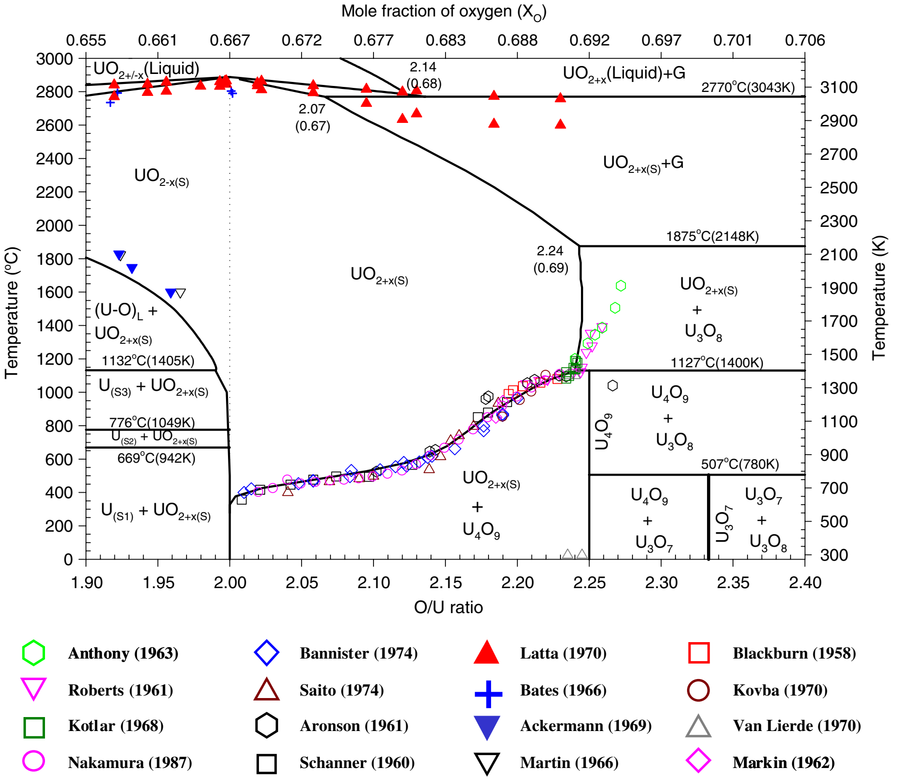

Fig. A.1. Calculated phase diagram for the U–O system, highlighting the UO_{2+x} region, shown against experimental phase boundary determinations.

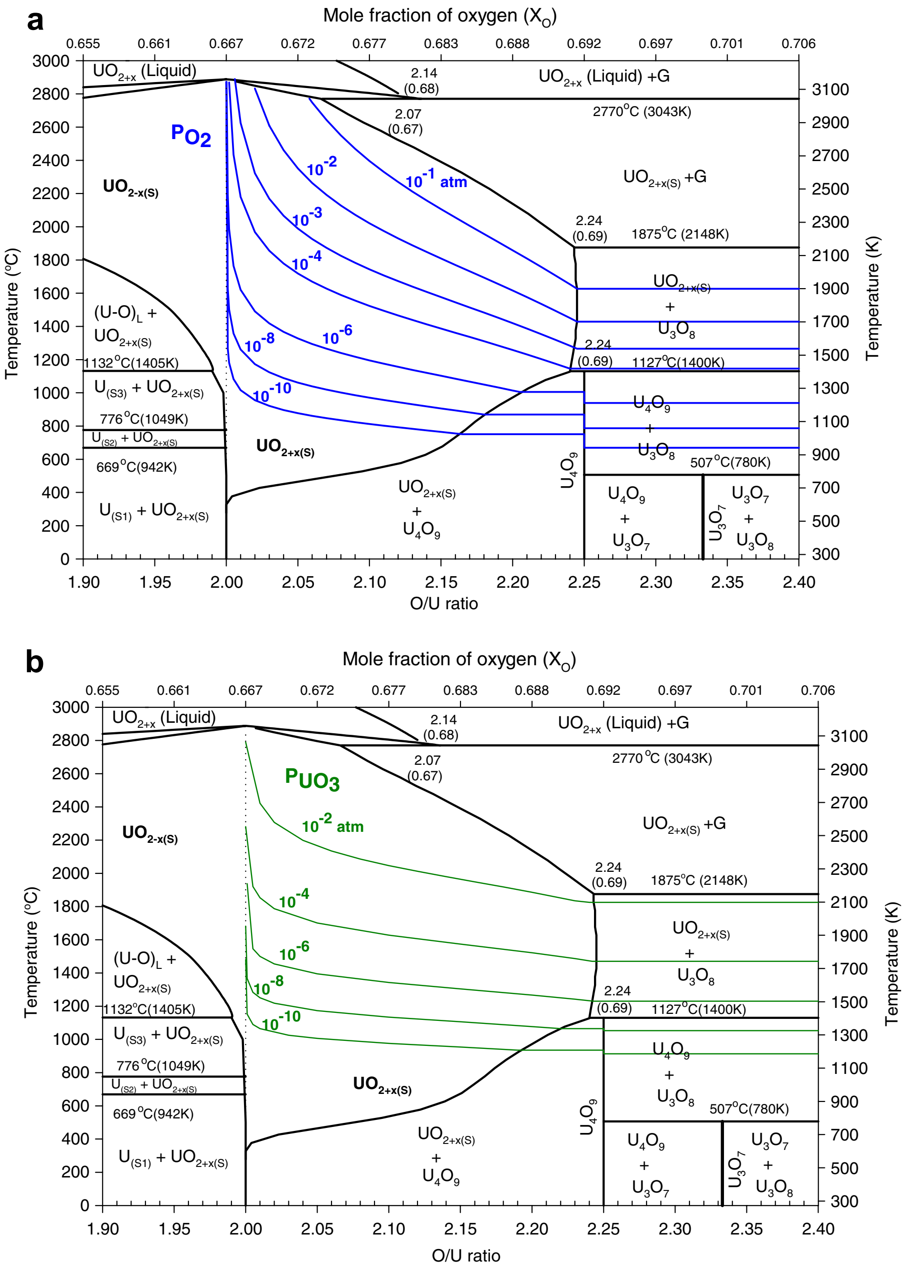

Fig. A.2. Calculated U–O binary phase diagram, highlighting the UO_{2+x} region, with isobaric lines of (a) oxygen and (b) UO_3 partial pressure.

Eq. (40) is in excellent agreement with the thermodynamic treatments of Lindemer–Besmann [53] and Blackburn [54]. Similarly, using properties for heavy water, the (D_2/D_2O) variation of the UO_{2+x} non-stoichiometry is [52]:

$$\log\left(\frac{p_{D_2}}{p_{D_2O}}\right) = \log\left(\frac{p_{H_2}}{p_{H_2O}}\right) + 1.76985 - \frac{333.783}{T} - 0.488145\log(T). \qquad (41)$$

These expressions are shown as they relate to the U–O phase diagram in Fig. A.3.

Using Eq. (40), a closed-form solution for the equilibrium stoichiometry deviation x_e is possible as a function of T and the hydrogen-to-steam partial pressure ratio ($q/(1-q)$) as shown in Eq. (12)). Eqs. (40) and (41) are only valid above certain minimum ratios of H_2/H_2O (or D_2/D_2O) as compared to the complete treatment for the U–O–H

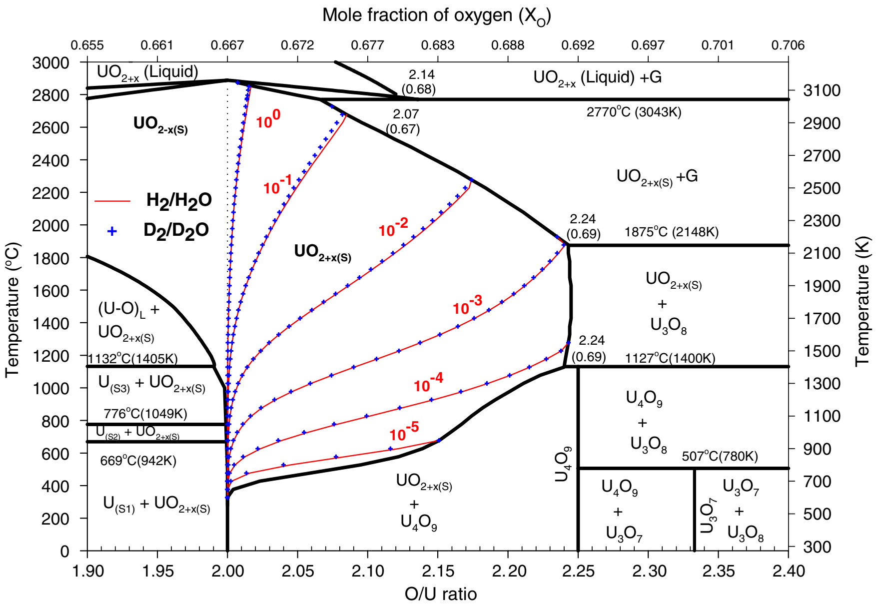

Fig. A.3. Calculated U–O binary phase diagram with lines of constant H_2/H_2O and points of constant D_2/D_2O ratios as calculated from Eqs. (40) and (41).

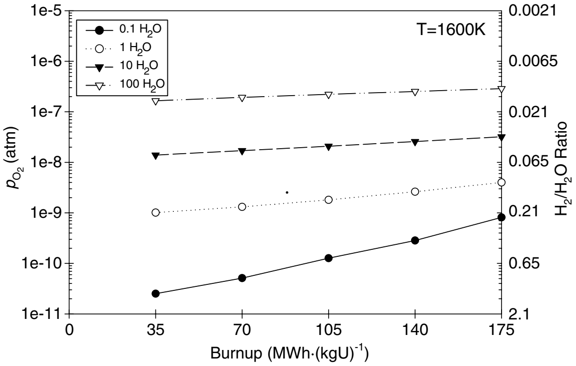

Fig. A.4. Oxygen partial pressure for various amounts of steam for a typical CANDU fuel element with burnup.

and U–O–D system. Therefore, an upper bound (that is a function of temperature) can be placed on these equations in accordance with the phase diagram boundaries.

Finally, the thermodynamic treatment of the U–O system in Fig. A.1. provides a model for oxidized UO_2 assuming fresh fuel. However, fission products and actinides are produced with burnup. Most fission product elements will form compounds with oxygen; this will affect the oxygen potential within the fuel. However, the current thermodynamic treatment can be extended to include fission products and actinides, which has the further advantage over earlier correlations of oxygen potential (e.g., the Lindemer and Besmann treatment) in that a multi-component Gibbs energy minimization calculation can be performed so that the influence of fuel burnup on the fuel oxygen potential can be assessed [55]. For instance, as shown in Fig. A.4, for a typical discharge burnup of ~175 MWh $(kgU)^{-1}$ for CANDU fuel reacting in the presence of increasing amounts of steam (0.1–100 mol H_2O), such calculations show that the effect of fission products on the fuel oxygen potential is small for the expected hydrogen-to-steam partial pressure ratio in Fig. A.3. This result is also consistent with the work of Park et al., which shows little change in the oxygen potential of intact fuel from 0 to 5 at.% burnup [56]. Burnup effects can therefore be neglected in the current thermodynamic treatment for the prediction of x_e in Eq. (12).

A.2. U–O–H_2O Pourbaix diagram

The thermodynamic model can also be applied to understand the fuel oxidation behaviour in the storage bays. In particular, Pourbaix diagrams of redox potential, E_h, versus pH are an important method for understanding aqueous chemical behaviour [57]. The Uranium Pourbaix diagram at 298.15 K, covering the range of redox potential pertinent to fuel oxidation behaviour, is shown in Fig. A.5. The details of the diagram development via Gibbs

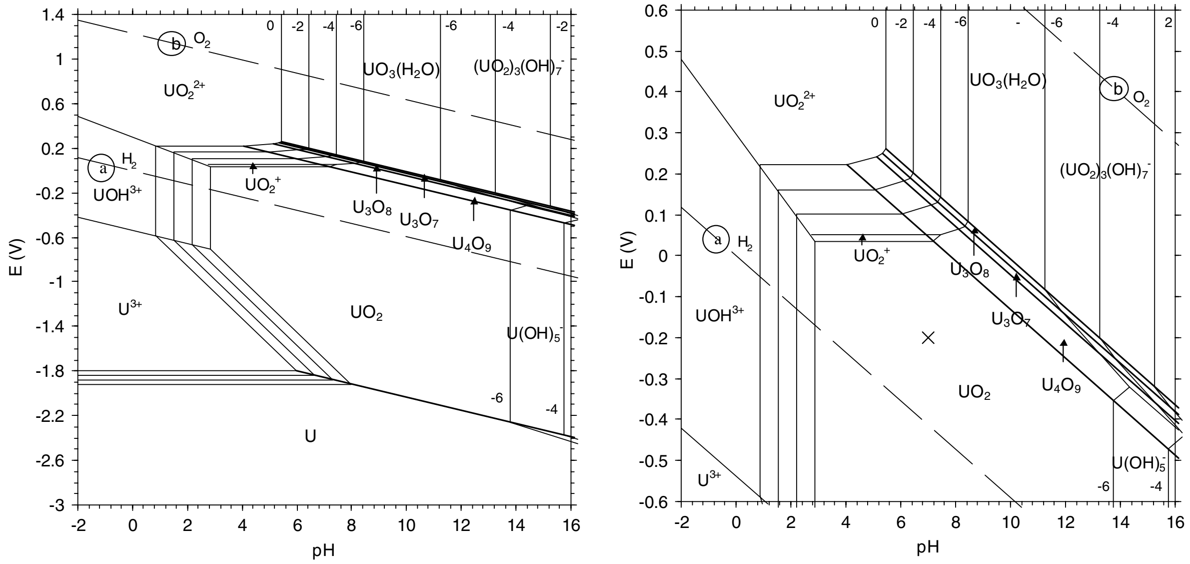

Fig. A.5. FACT generated U–H_2O Pourbaix diagram at 298.15 K.

energy minimization are given in Ref. [58]. The data for UO_2, U_4O_9, U_3O_7 and U_3O_8 are the same as those used for the U-O binary phase diagram in Fig. A.1. Placed on the diagram for reference are dashed lines (a) and (b) corresponding to redox potentials associated with hydrogen and oxygen saturation (at 1 atm), respectively. Thus, this methodology provides a means to assess fuel oxidation behaviour of defective fuel during long-term storage in the fuel bays, where the bay water is in near equilibrium with air (see Section 4.3.5).

Appendix B. Estimation of parameters ε and σ_f

The number of fuel cracks n (during operation) has been correlated by Wood et al. to the linear element power P (in kW m^{-1}) as $n = P/2$ [2,70]. Assuming that a crack penetrates through the entire fuel stack length ℓ, and it has a thickness $s = a \cdot \theta \sim$ 44 μm from post irradiation examination, the volume of a single crack from elementary geometry is $\frac{1}{2}a^2\theta \cdot \ell$ where θ is the crack angle (in radians). Thus, considering a simple crack representation with n symmetrical cracks in Fig. B.1:

$$\varepsilon = \frac{V_{\text{crack}}}{V_{\text{fuel}}} = \frac{\frac{n\theta\ell}{2}\{a^2 - a^2_{\text{plastic}}\}}{\pi a^2 \ell} = \frac{Ps\{a^2 - a^2_{\text{plastic}}\}}{4\pi a^3} = \frac{3}{16}\frac{Ps}{\pi a}. \tag{42}$$

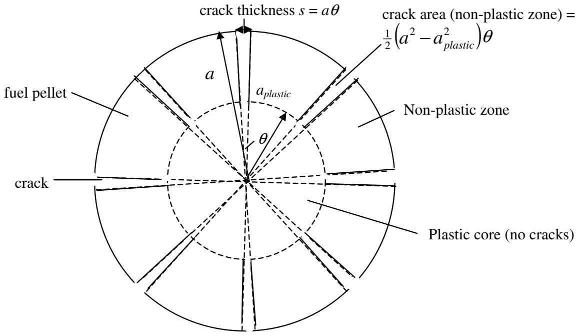

Fig. B.1. Schematic cross section of a cracked fuel pellet.

Here it is assumed that the cracks do not penetrate into the plastic zone at radius a_{plastic}, where $a_{\text{plastic}} \sim a/2$ at a typical linear heat rating of 35 kW m^{-1}. Thus, at this linear heat rating, ε is evaluated as ~1.5%. Moreover, it follows that:

$$\sigma_f = \frac{S_{\text{crack}}}{V_{\text{fuel}}} = \frac{n\ell 2(a - a_{\text{plastic}})}{\pi a^2 \ell} = \frac{P}{2\pi a} \tag{43}$$

yielding a value of $\sigma_f \sim 910\ m^{-1}$ at 35 kW m^{-1}. These values are typical of that assumed in Table 1 (which are used for all simulations).

In addition, the ratio of the volume of cracks to the volume of the gap is:

$$\frac{V_{\text{crack}}}{V_{\text{gap}}} = \frac{\frac{n\theta a^2}{2}\left(1 - \frac{a^2_{\text{plastic}}}{a^2}\right)}{2\pi a t_g} = \frac{3}{16}\frac{n(\theta a)}{\pi t_g}, \tag{44}$$

where t_g is $\sim$10–20 μm based on a fuel performance calculation with the ELESIM code. [2] Using the above data for an element at 35 kW m^{-1} (i.e., $n = 35/2 \sim 17$ cracks, $\theta\ a \sim 44\mu m$ and $a_{\text{plastic}} \sim a/2$), the crack volume is estimated with Eq. (44) to be comparable to that of the gap (i.e., $V_{\text{crack}} \sim 3V_{\text{gap}}$). Moreover, the CANDU fuel design also has thin sheathing that can accommodate expansion from fuel cracking and relocation, i.e., the In-Reactor Diameter Measuring Rig (IRDMR) has been used for a direct in-reactor measurement of CANDU fuel relocation, where a diametral relocation of approximately 30 μm was observed [71]. Hence, the simple crack model appears to be consistent with the observed in-reactor behaviour.

References

[1] B.J. Lewis, R.D. MacDonald, N.V. Ivanoff, F.C. Iglesias, Nucl. Technol. 103 (1993) 220.

[2] B.J. Lewis, F.C. Iglesias, D.S. Cox, E. Gheorghiu, Nucl. Technol. 92 (1990) 353.

[3] W. Hüttig, H. Zänker, M. Forberg, J. Nucl. Mater. 175 (1990) 147.

[4] D.R. Olander, Nucl. Technol. 74 (1986) 215.

[5] D.R. Olander, Y.S. Kim, W. Wang, S.K. Yagnik, J. Nucl. Mater. 270 (1999) 11.

[6] B.J. Lewis, B. Szpunar, F.C. Iglesias, J. Nucl. Mater. 306 (2002) 30.

[7] B.J. Lewis, W.T. Thompson, F. Akbari, D.M. Thompson, C. Thurgood, J. Higgs, J. Nucl. Mater. 328 (2004) 180.

[8] Hj. Matzke, Radiat. Eff. 53 (1980) 219.

[9] H. Kleykamp, J. Nucl. Mater. 84 (1979) 109.

[10] K. Une, Y. Tominaga, S. Kashiba, J. Nucl. Sci. Technol. (Jpn.) 28 (1991) 409.

[11] Hj. Matzke, J. Nucl. Mater. 208 (1994) 18.

[12] Hj. Matzke, J. Nucl. Mater. 223 (1995) 1.

[13] C.T. Walker, V.V. Rondinella, D. Papaioannou, S. Van Winckel, W. Goll, R. Manzel, J. Nucl. Mater. 345 (2005) 192.

[14] K. Une, M. Imamura, M. Amaya, Y. Korei, J. Nucl. Mater. 223 (1995) 40.

[15] M. Imamura, K. Une, J. Nucl. Mater. 247 (1997) 131.

[16] R.A. Verrall, Z. He, J. Mouris, J. Nucl. Mater. 344 (2005) 240.

[17] R.B. Bird, W.E. Stewart, E.N. Lightfoot, Transport Phenomena, Wiley, New York, 1960.

[18] R.C. Reid, J.M. Prausnitz, B.E. Poling, The Properties of Gases and Liquids, McGraw-Hill Book Company, New York, 1987.

[19] G.W. Parry, P.G. Smerd, Review of PWR Fuel Rod Waterside Corrosion Behavior, NP-1472, Electric Power Research Institute, August 1980.

[20] B.J Lewis, W.T. Thompson, J. Higgs, F. Akbari, C. Thurgood, Part II: Modeling of Fuel Oxidation and Fission Product Release Behavior for Defective Fuel, Light Water Reactor Fuel Performance Conference, Orlando, Florida, September 19–22, 2004.

[21] B.R. Munson, D.F. Young, T.H. Okiishi, Fundamentals of Fluid Mechanics, 2nd Ed., John Wiley, Toronto, 1994.

[22] B.J. Lewis, H.W. Bonin, J. Nucl. Mater. 218 (1994) 42.

[23] F. Ewart, K. Lassmann, Hj. Matzke, L. Manes, A. Saunders, J. Nucl. Mater. 124 (1984) 44.

[24] M.H. Rand, T.L. Markin, Thermodynamics of Nuclear Materials, 1967, in: Proc. IAEA Symp., Vienna 1968, p. 637.

[25] C. Sari, G. Schumacher, J. Nucl. Mater. 61 (1976) 192.

[26] K. Lassmann, J. Nucl. Mater. 150 (1987) 10.

[27] D.S. Cox, F.C. Iglesias, C.E.L. Hunt, N.A. Keller, R.D. Barrand, J.R. Mitchell, R.F. O'Connor, Oxidation of UO_2 in air and steam with relevance to fission product releases, in: Proc. Symp. on Chemical Phenomena Associated with Radioactivity Releases during Severe Nuclear Plant Accidents, NUREG/CP-0078, Anaheim, CA, US Nuclear Regulatory Commission, 1986, p. 2.

[28] D.S. Cox, F.C. Iglesias, C.E.L. Hunt, R.F. O'Connor, R.D. Barrand, High temperature oxidation behaviour of UO_2 in air and steam, in: Proc. Int. Symp. on High-Temperature Oxidation and Sulphidation Process, Hamilton, Ontario, Canada, August 26–30, 1990.

[29] D.R. Olander, J. Nucl. Mater. 252 (1998) 121.

[30] J. Abrefah, A. de Aguiar Braid, W. Wang, Y. Khalil, D.R. Olander, J. Nucl. Mater. 208 (1994) 98.

[31] J.A. Meachen, Nucl. Energy 28 (4) (1989) 221.

[32] J.C. Ramirez, M. Stan, P. Cristea, J. Nucl. Mater. 359 (2006) 174.

[33] Hj. Matzke, Diffusion in Ceramic Oxide Systems, in: I.J. Hastings (Ed.), Fission-Product Behavior in Ceramic Oxide Fuel, Advances in Ceramics, vol. 17, American Ceramic Society, Columbus, Ohio, 1986, p. 1.

[34] W.T. Thompson, B.J Lewis, F. Akbari, D.M. Thompson, Part I: Thermodynamic Modeling of Uranium Oxidation in Support of Fission Product Transfer from Defective Fuel, in: Light Water Reactor Fuel Performance Conference, Orlando, Florida, September 19–22, 2004.

[35] J.L. Bates, J. Am. Ceram. Soc. 49 (7) (1966) 396.

[36] R.G. Ackermann, E.G. Rauh, M.S. Chandrasekharaiah, J. Phys. Chem. 34 (4) (1969) 762.

[37] R.K. Edwards, A.E. Martin, Thermodynamics of Nuclear Materials, vol. 2, IAEA, Vienna, 1966.

[38] B.E. Schaner, J. Nucl. Mater. 2 (1960) 110.

[39] L.E.J. Roberts, A.J. Walter, J. Inorg. Nucl. Chem. 22 (1961) 213.

[40] S. Aronson, J.E. Rulli, B.E. Schaner, J. Phys. Chem. 35 (4) (1961) 1382.

[41] M.J. Bannister, W.J. Buykx, J. Nucl. Mater. 55 (1974) 345.

[42] Y. Saito, J. Nucl. Mater. 51 (1974) 112.

[43] A. Nakamura, T. Fujino, J. Nucl. Mater. 149 (1987) 80.

[44] R.E. Latta, R.E. Fryxell, J. Nucl. Mater. 35 (1970) 195.

[45] A.M. Anthony, R. Kiyoura, T. Sata, J. Nucl. Mater. 10 (1) (1963) 8.

[46] A. Kotlar, P. Gerdanian, M. Dode, J. Chim. Phys. 65 (1968) 687.

[47] P.E. Blackburn, J. Phys. Chem. 62 (8) (1958) 897.

[48] L.M. Kovba, (Presented by Academician V. I. Spitsyn, January 26, 1970) Translated from Doklady Akademii Nauk SSSR, 194 (1) September(1970), 98.

[49] W. Van Lierde, J. Pelsmaekers, A. Lecocq-Robert, J. Nucl. Mater. 37 (1970) 276.

[50] T.L Markin, R.J. Bones, Determination of changes in free energy for uranium oxides using a high temperature galvanic cell, part 1, U.K.A.E.A., Report AERE-R 4042, 1962.

[51] P.-Y. Chevalier, E. Fischer, B. Cheynet, J. Nucl. Mater. 303 (2002) 1.

[52] C.W. Bale, A.D. Pelton, W.T. Thompson, Facility for the Analysis of Chemical Thermodynamics, McGill University and École Polytechnique, 1995.

[53] T.B. Lindemer, T.M. Besmann, J. Nucl. Mat. 130 (1985) 473.

[54] P.E. Blackburn, J. Nucl. Mater. 46 (1973) 244.

[55] M.H. Kaye, C. Morrison, J. Higgs, F. Akbari, B.J. Lewis, W.T. Thompson, Towards a First Principles Model of CANDU Fuel Phase Equilibrium, in: Proc. 9th Int. Conf. on CANDU Fuel, Belleville, ON, September 17–21, 2005.

[56] K. Park, M-S. Yang, H-S. Park, J. Nucl. Mater. 247 (1997) 116.

[57] M. Pourbaix, Atlas of Electrochemical Equilibria in Aqueous Solutions, Pergamon, New York, 1966.

[58] B.J. Lewis, W.T. Thompson, F. Akbari, C. Morrison, A. Husain, J. Nucl. Mater. 340 (2005) 69.

[59] J.D. Higgs, Modelling oxidation behaviour in operating defective nuclear reactor fuel elements, PhD Dissertation, Royal Military College, January 2006.

[60] D.R. Olander, Fundamental aspects of nuclear reactor fuel elements, TID-26711-p1, US Department of Energy, 1976.

[61] D.G. Martin, J. Nucl. Mater. 152 (1988) 94.

[62] P.G. Lucuta, Hj. Matzke, I.J. Hastings, J. Nucl. Mater. 232 (1996) 166.

[63] W.E. Ellis, J.D. Porter, T.L. Shaw, The Effect of Oxidation, Burnup and Poisoning on the Thermal Conductivity of UO_2: A Comparison of Data with Theory, in: Proc. International Topical Meeting on Light Water Reactor Fuel Performance, Park City, Utah, April 10–13, 2000, p. 715.

[64] C. Ronchi, M. Sheindlin, M. Musella, G.J. Hyland, J. Appl. Phys. 85 (1999) 776.

[65] P.G. Lucuta, R.A. Verrall, Hj. Matzke, J. Nucl. Mater. 223 (1995) 5160.

[66] J.K. Fink, J. Nucl. Mater. 279 (2000) 1.

[67] I.J. Hastings, L.E. Evans, J. Am. Ceram. Soc. (March–April) (1979) 217.

[68] W. Wiesenack, Thermal performance of high burnup fuel – in-pile temperature data and analysis, in: Light Water Reactor Fuel Performance Conference, Portland, Oregon, March 2–6, 1997, p. 507.

[69] W. Wiesenack, T. Tverberg, Assessment of UO_2 conductivity degradation based on in-pile temperature data, in: Light Water Reactor Fuel Performance Conference, Park City, Utah, April 10–13, 2000.

[70] J.C. Wood, B.A. Surette, I. Aitchison, W.R. Clendening, J. Nucl. Mater. 88 (1980) 81.

[71] P.J. Fehrenbach, P.A. Morel, R.D. Sage, Nucl. Technol. 56 (1982) 112.

[72] R.A. Verrall, J. Mouris, Z. He, O/M measurement technique, in: Eighth International Conference on CANDU Fuel, Honey Harbour, Ontario, September 21–24, 2003.

[73] Z. He, R. Verrall, J. Mouris, C. Buchanan, Private Communication (April) (2003).

[74] J. Mouris, private communication (October) (2004).

[75] H. Kleykamp, J. Nucl. Mater. 131 (1985) 221.

[76] J.O. Hirschfelder, C.F. Curtiss, R.B. Bird, Molecular Theory of Gases and Liquids, John Wiley, New York, 1964.

[77] D. Manara, C. Ronchi, M. Sheindlin, M. Lewis, M. Brykin, J. Nucl. Mater. 342 (2005) 148.

[78] S. Whillock, J.H. Pearce, J. Nucl. Mater. 175 (1990) 121.

[79] J.M. Markowitz, Internal zirconium hydride formation in zircaloy fuel element cladding under irradiation, WAPD-TM-351, Bettis Atomic Power Laboratory, May 1963.

[80] K. Naito, J. Nucl. Mater. 51 (1) (1974) 126.

[81] T. Ishii, K. Naito, K. Oshima, Solid State Commun. 8 (1970) 677.

[82] F. Grønvold, J. Inorg. Nucl. Chem. 1 (1955) 357.

[83] H.-R. Wenk, L. Lutterotti, S. Vogel, Nucl. Instrum. and Meth. A 515 (2003) 575.

[84] Los Alamos Neutron Science Center Website, www.lansce.lanl.gov.

[85] J. Higgs, W.T. Thompson, B.J. Lewis, S. Vogel, Kinetics of precipitation of U_4O_9 from hyperstoichiometric UO_{2+x}, in: TMS Space Reactor Fuels and Materials Symposium, San Antonio, Texas, March 12–16, 2006.

[86] M.T. Hutchings, J. Chemical Society. Faraday Trans. 283 (1987) 1083.

[87] J.S. Kim, Y.-N. Choi, C.H. Lee, S.-H. Kim, Y.-W. Lee, J. Korean Ceram. Soc. 38 (11) (2001) 967.

[88] N. Masaki, K. Doi, Acta Crystallogr. B28 (1972) 785.

[89] J. Belle (Ed.), Uranium Dioxide: Properties and Nuclear Applications, Naval Reactors, Division of Reactor Development, USAEC, 1961.

[90] S. Aronson, R.B. Roof, J. Belle, J. Chem. Phys. 27 (1957) 137.

[91] H.R. Hoekstra, A. Santoro, S. Siegel, J. Inorg. Nucl. Chem. 18 (1961) 166.

[92] K.A. Simpson, P. Wood, Uranium Dioxide Fuel Oxidation below 350 °C, in: Proc. NRC Workshop on Spent Fuel/Cladding Reaction during Dry Storage, Gaithersburg, MD, (1983) (NUREG/CP-0049), 70.

[93] J. Novak, I.J. Hastings, E. Mizzan, R.J. Chenier, Nucl. Technol. 63 (1983) 254.

[94] I.J. Hastings, E. Mizzan, A.M. Ross, J.R. Kelm, R.J. Chenier, D.H. Rose, J. Novak, Nucl. Technol. 68 (1985) 40.

[95] I.J. Hastings, E. Mizzan, J.R. Kelm, R.E. Moeller, J. Novak, Nucl. Technol. 68 (1985) 418.

[96] I.J. Hastings, D.R. McCracken, E. Mizzan, R.D. Barrand, J.R. Kelm, K.E. Nash, J. Novak, Nucl. Technol. 70 (1985) 268.

[97] R.E. Einziger, R.E. Woodley, Predicting spent fuel oxidation states in a tuff repository, in: Proc. Workshop on Chemical Reactivity of Oxide Fuel and Fission Product Release, Vol. 2, Berkeley Nuclear Laboratories, Berkeley, Gloucestershire, England, 7–9 April 1987, p. 281.

[98] K.M. Wasywich, C.R. Frost, Update on the Canadian experimental program to evaluate used-fuel integrityunder dry-storage conditions, in: Proc. Second Int. Conf. CANDU Fuel, Pembroke, Ontario, 1989, 312.

[99] K.M. Wasywich, W.H. Hocking, D.W. Shoesmith, P. Taylor, Nucl. Technol. 104 (1993) 309.

[100] P. Taylor, R.J. Lemire, D.D. Wood, Nucl. Technol. 104 (1993) 164.

[101] S. Sunder, N.H. Miller, J. Nucl. Mater. 231 (1996) 121.

[102] P. Taylor, J. Nucl. Mater. 344 (2005) 206.

[103] R.J. McEachern, P. Taylor, J. Nucl. Mater. 254 (1998) 87.

[104] A. Leenaers, L. Sannen, S. Van den Berghe, M. Verwerft, J. Nucl. Mater. 317 (2003) 226.

[105] P. Taylor, D.D. Wood, D.G. Owen, W.G. Hutchings, A.M. Duclos, Microstructure and phase relationship of crystalline oxidation products formed on unused CANDU fuel exposed to aerated steam and water near 200 °C, Atomic Energy of Canada Limited report AECL-10476, COG-91-292, 1991.

[106] P. Taylor, D.D. Wood, A.M. Duclos, D.G. Owen, J. Nucl. Mater. 168 (1989) 70.

[107] P. Taylor, D.D. Wood, D.G. Owen, G.-I. Park, J. Nucl. Mater. 183 (1991) 105.

[108] P. Taylor, D.D. Wood, D.G. Owen, J. Nucl. Mater. 223 (1995) 316.

[109] C.R. Frost, K.M. Wasywich, UO_2 oxidation in air at 50 °C to 400 °C and the implications for CANDU irradiated fuel dry storage, in: Proc. Workshop on Chemical Reactivity of Oxide Fuel and Fission Product Release, Vol. 2, Berkeley Nuclear Laboratories, Berkeley, Gloucestershire, England, 7–9 April, 1987, p. 319.

[110] K. Une, S. Kashibe, J. Nucl. Mater. 232 (1996) 240.